ABSTRACT

Metal Ion Assisted Unimolecular Decomposition of Gaseous Organometallic Complexes: Acquisition of Reaction Rate Constants and Dynamics of the Dissociative Mechanism

Otsmar J. Villarroel, Ph.D.

Mentor: Darrin J. Bellert, Ph.D.

Reaction rate constants have been acquired for the transition metal ion assisted decomposition of various organic molecules, and their deuterium labeled analogs in the gas phase. The metal ion activates organic bonds and mediates the formation of products. Thus, the transition metal cation lowers the bond activation energy requirements in these decomposition reactions making these systems model for catalysis. Catalytic reaction kinetics are not well understood and it is hoped that the resolved study of simpler catalytic models will further the development of the theoretical tools necessary to describe such mechanistic behavior at the molecular level.

Reaction rate constants for these model systems are measured using a custom-built molecular beam apparatus. The clusters are formed under supersonic expansion conditions and are bound by the charge-dipole electrostatic interaction between a transition metal cation and a polar organic molecule. The unimolecular decomposition occurs upon laser photon absorption by the jet-cooled cluster yielding a stable neutral molecule and corresponding ion.

This dissertation will focus on the unimolecular decomposition kinetics of the $Co^+$-Acetone cluster and its deuterium labeled analog. Rate constants are measured at well resolved cluster internal energies. The kinetic isotope effect (KIE) for each measurement was determined. Results are compared to the similar $Ni^+$-Acetone decomposition reactions, where the KIE was also measured. These two similar systems present rather different dissociation dynamics. Arguments based on the electronic structure of each ion explain this unique behavior between these similar systems.

DFT calculations are made on most systems presented in this dissertation. The most likely geometries and relative energies of the reactants, intermediates and products are determined. Such information specifies aspects of the reaction coordinate and leads to suggestions of mechanisms. This was primarily applied in the final chapter of this dissertation where preliminary results of $Ni^+$-assisted decomposition of cyclopentanone are presented. This system represents the group's first study of a ring-opening reaction.

Metal Ion Assisted Unimolecular Decomposition of Gaseous Organometallic Complexes: Acquisition of Reaction Rate Constants and Dynamics of the Dissociative Mechanism

by

Otsmar J. Villarroel, B.S.

A Dissertation

Approved by the Department of Chemistry and Biochemistry

_____
Patrick J. Farmer, Ph.D., Chairperson

Submitted to the Graduate Faculty of
Baylor University in Partial Fulfillment of the
Requirements for the Degree
of
Doctor of Philosophy

Approved by the Dissertation Committee

_____
Darrin J. Bellert, Ph.D., Chairperson

_____
Carlos E. Manzanares, Ph.D.

_____
John A. Olson, Ph.D.

_____
David E. Pennington, Ph.D.

_____
Kenneth T. Park, Ph.D.

Accepted by the Graduate School
December 2011

_____
J. Larry Lyon, Ph.D., Dean

*Page bearing signatures is kept on file in the Graduate School.*

TABLE OF CONTENTS

LIST OF FIGURES

LIST OF TABLES

# ACKNOWLEDGMENTS

First and foremost, I want to thank God for allowing me to accomplish this important goal in my life. I would like to thank my family for providing the constant love and moral. You represent everything for me. You are my inspiration and motivation. You are the best family in the world!

I would like to express my most sincere acknowledgment to Dr. Darrin J. Bellert, for his constant and unconditional support, encouragement, and extreme patience during my stay the group. Your energy, love, talent, and enthusiasm in both teaching and in research are an example to be followed. Thank you for your patience in reading this dissertation and for your assistance in the preparation of other papers and presentations. Your guidance is truly invaluable. Also, I would like to thank Ronda Bellert for opening the doors of her house to me on different occasions and making me feel like a member of her family.

I would like to thank Dr. Carlos E. Manzanares for giving me the opportunity to study at Baylor University. Thank you for your help and for taking care of us all of the time. Further acknowledgments also go to my dissertation committee: Dr. Carlos E. Manzanares, Dr. John A. Olson, Dr. David Pennington and Dr. Kenneth T. Park for their dedication and for donating part of their time to review my work and make valuable comments.

To the first two Bellert Group members: Dr. Vannesa Castleberry and Dr. S.Jason Dee for their guidance, training time, tips, patience and friendship during my first few years in the group. You both made me feel welcome upon my arrival to the group.

Together, you guys helped to build some of the best equipment in the world. Thank you for your assistance and I wish the best for you both in your still young professional careers.

I would also like to thank my Venezuelan and Latin friends at Baylor, who have helped me, complete this journey and made me feel like part of a family away from home. You have made a difference in my life. Thank you for your unconditional support and for sharing unforgettable moments with me. I wish the best for all of you. Also, I want to thank my friends in Venezuela, who have been with me these past years. Thank guys for showing me that despite a long distance; a strong friendship is still possible. God bless you guys!

To the friends I have made here at Baylor, thank you for everything! To my research fellows: J.R. and Adam thank you for your help and I hope you both take this research group to new heights. A special thanks to Dr. Ivanna E. Laboren, for being a good friend, roommate, and excellent lab partner during my years here at Baylor. Thank for you advices, help analyzing data and encouraging me to complete my dissertation and for sharing this journey with me. I wish the best for you in your future! To Katie (Katy) Benjamin for spending your time reading and editing this dissertation and other papers, even when you were too busy with your classes. You are an outstanding student. Thank you a lot for your help with the language. I wish the best for you in your life.

My gratitude also goes to the staff to the Chemistry and Biochemistry Department at Baylor, in particular to Nancy Kallus and Virginia Hynek. You both have always helped me to resolve any problem or concern I had related with administration problems or order problems. Thanks a lot!

Finally, I want to thank Monica Roman for being patient and for her constant support, enthusiasm and love. Thanks for all of you support and encouraging words during my time here at Baylor. Thanks for everything you have done for me!

This research would not be possible without financial support from the ACS Petroleum Research Fund, the Baylor University Research Committee and the Vice Provost for Research.

A mi familia por su amor y soporte

A mi abuela Magdalena Larez, Lina y Carlucho por guiarme desde el cielo

# CHAPTER ONE

## Introduction

### *Bond Activation of Organic Molecules by Transition Metal Ions in the Gas Phase: Catalytic- Styled Reactions*

Transition metal ions have proven to be highly reactive in the gas phase.[1-11] Studies showing this reactivity between gaseous transition metal ions with a variety of organic species have been accomplished using ion cyclotron resonance (ICR) mass spectrometry,[12-24] and ion beam techniques using tandem mass spectrometry.[25-47] A variety of fundamental thermodynamic, kinetic, and mechanistic information about gaseous organometallic chemical reactions have been obtained. Transition metal ions can facilitate ligand-substitution reactions, dehydrogenate alkyl halides, dehydrate alcohols, induce $H_2$ elimination from organic compounds, cleave C-X (X=O, N, S, halogens) bonds in polar compounds and C-C and C-H bonds in hydrocarbons, etc. Theoretical investigations have complimented these experimental studies by suggesting possible mechanisms through the calculation of reaction potential energy surfaces.[48-54]

Often, the interaction between a transition metal cation and an organic molecule lowers the activation energy requirements to bond cleavage reactions. Thus, these systems may be viewed as models for catalysis. Therefore, it is not surprising that considerable research has been devoted to determine the kinetic barriers associated with C-C and C-H bond activation processes.

In 1975, Allison and Ridge[15] reported the first reactions of metal containing ions with organic molecules. Here, organic bonds were cleaved and metal-carbon bonds formed. They reported second order rate constants for the reactions,

$$M^+ + CH_3I \longrightarrow M^+I + CH_3 \qquad \text{(rxn 1)}$$
$$\longrightarrow M^+CH_3 + I \qquad \text{(rxn 2)}$$

where M= Co and Fe. While products containing M-C and M-X bonds were observed with methyl iodide, only one product was observed in the reactions of $Fe^+$ and $Co^+$ with methyl bromide. They concluded that such differences are due to the exothermic formation of $M^+CH_3$ from $CH_3I$ while the analogous process, forming $M^+CH_3$ from $CH_3Br$, is not observed because it is endothermic. In 1976 Allison and Ridge[16] proposed a mechanism for the reaction of transition metal ions with alkyl halides and alcohols in the gas phase. This mechanism involves metal ion insertion into the polar bond, followed by a β-H shift. This mechanism appears to be the only way to explain the formation of $M^+CH_3$ from $CH_3I$ in rxn 2.

Subsequent (ICR) studies reported results from the gas phase chemistry of a variety of metal ions with alkyl halides and alcohols.[55-57] Many of these papers reported H-X elimination reactions with alkyl halides and $H_2O$ elimination from alcohols. Additionally, halide and halogen transfer reactions were observed. These studies demonstrated that not all first row transition metal atomic ions react in the same way. Consider the case of $Fe^+$, $Co^+$, and $Ni^+$; these ions are believed to react with alkyl halides and alcohols by the same mechanism. Despite this similarity the product distributions are unique for each metal ion reaction. This difference can be attributed to factors such as the change in the total energy content; or to the effects of spin, spin orbit level, and electronic configuration of the ions.[59-61]

Although the metal insertion and β-H shift mechanism was generally considered valid, early ICR studies of transition metals reacting with alkyl halides and alcohols showed that the reaction with each metal ion was unique. Therefore, subsequent studies of the gas phase chemistry of metal ions with polar, non-polar, and functionalized organic molecules was sought to establish a fundamental understanding of product distributions and ion reactivity. This chapter briefly discusses reactions of several transition metal ions with alkanes, alkenes and various carbonyl containing organic compounds.

Gas phase reactions between the first row transition metal ions and alkanes were intriguing because of the obvious simplicity and implications for catalysis. [11-12, 25-27, 29, 31-33] Such reactions represent one of the simplest models for the competition between C-H and C-C bond activation. Atomic transition metal ions react with alkanes by oxidative and reductive elimination processes that involve the formation of species such as $M^+H_2$, $HM^+R$, and $M^+R_2$ where R is an alkyl group. In general, as is shown in rxn 3, oxidative addition of a metal ion across a C-C bond is postulated as the initial step in the cleavage of alkanes. This is followed by a β-hydride shift onto the metal and then onto the alkyl portion, resulting in reductive elimination of an alkane and formation of a primary olefin metal complex. Oxidative addition of a metal across a C-H bond is proposed as the initial step in the dehydrogenation of alkanes and is shown in rxn 4. This is followed by a β-hydride shift onto the metal with subsequent reductive elimination of hydrogen (a 1,2 elimination process) and formation of an olefin-metal complex. However, Beauchamp et al.[12] reported that $Ni^+$ dehydrogenates alkanes larger than propane by a highly specific 1,4 elimination mechanism. Rxn 5 displays a mechanism that involves initial oxidative addition of $Ni^+$ across an internal C-C bond. This is followed by two successive β-hydride shifts onto the metal with reductive elimination of hydrogen producing a bis-

olefin complex. Later studies that involve $Co^+$ and $Fe^+$ reactions with alkanes were reported. The studies show that these two metals produce both cleavage and dehydrogenation products as well. Linear alkanes larger than butane can be cleaved by $Fe^+$, $Co^+$, and $Ni^+$ to produce $M^+C_4H_8$[29] (reported as a bisolefin complex). The $M^+C_4H_8$ ion has been proposed as an intermediate structure in the reactions of cycloalkanes and cyclic ketones with transition metal ions.[12, 20, 26, 29, 47] However, the proposed structure for this intermediate is a cyclic. These types of intermediates are called metallacycles and will be discussed in greater detail in chapter five.

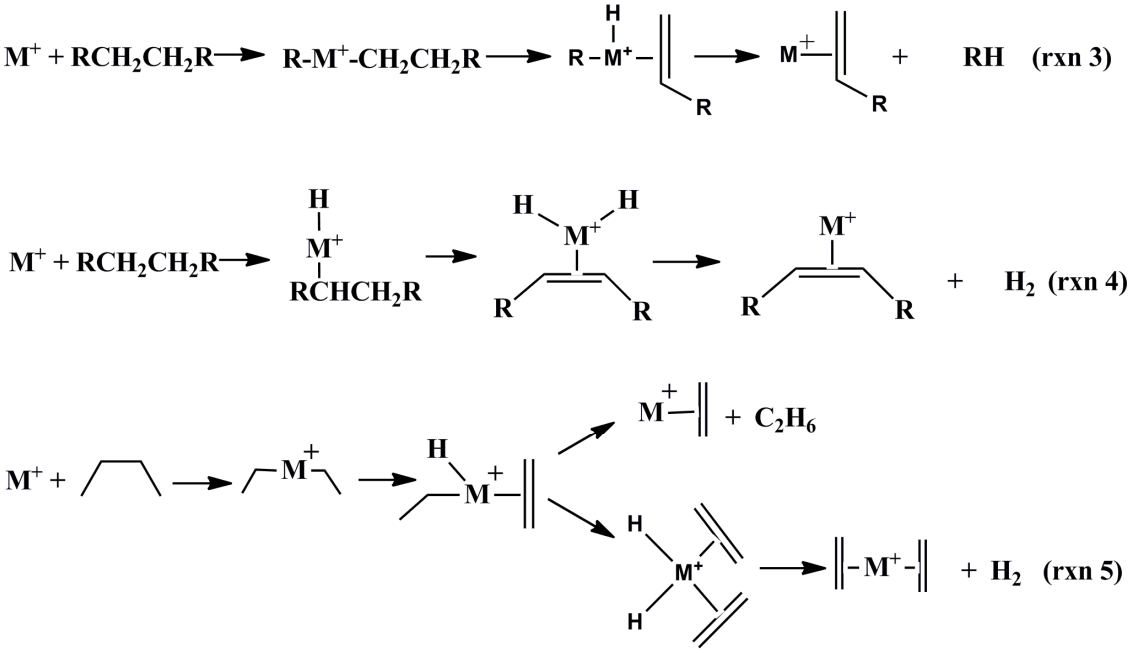


Studies of gas phase transition metal ion reactions with olefins have also been reported.[14, 25, 28] Ridge[14] and Beauchamp[25] have studied such reactions between olefins with $Ti^+$ and $Co^+$, respectively. Dehydrogenation reactions dominated for $Ti^+$ while both dehydrogenation and C-C bond cleavage processes were observed for $Co^+$. In those studies, the metal ion was proposed to initially interact with the olefin double bond to form an activated complex which then eliminates hydrogen, small alkanes, or small

olefins. Rxn 6 shows the products of the reaction between $Co^+$ and 1-pentene. $Co^+$ eliminates hydrogen, methane and small alkanes from 1-pentene where the production of $C_2H_4$ and $C_3H_6$ dominates the product distribution.

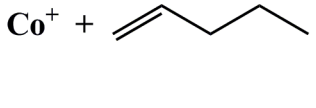

$$\begin{array}{l} Co^+C_5H_8 + H_2 \\ Co^+C_4H_6 + CH_4 \\ Co^+C_3H_6 + C_2H_4 \\ Co^+C_2H_4 + C_3H_6 \end{array} \qquad \textbf{(rxn 6)}$$

Since 1975 papers have appeared discussing the chemistry of various gaseous transition metal ions with a variety of different compounds other than alkanes and alkenes. In 1981 Freiser et al.[19] reported the chemistry of a variety of ethers with $Fe^+$. Small ethers form expected products following $Fe^+$ insertion into the polar C-O bond (rxn 7). It is interesting that during reactions between $Fe^+$ and ethers containing larger alkyl chains, both C-O and C-C activation appears possible. However, C-O activation dominates the product distribution.

$$Fe^+ + C_2H_5OC_2H_5 \longrightarrow C_2H_5Fe^+OC_2H_5 \longrightarrow \begin{array}{l} Fe^+C_2H_4 + C_2H_5OH \\ Fe^+C_2H_4O + C_2H_6 \\ Fe^+C_2H_5 + C_2H_4 \end{array} \qquad \textbf{(rxn 7)}$$

Small ketones, esters, aldehydes, and acids react with transition metal ions through a common mechanism. Metal insertion into bonds adjacent to the carbonyl group dominates. This is generally followed by an α-alkyl shift from the RCO group and a β-H shift.

There have been several studies of the gas phase reactions of metal ions with aldehydes and ketones. Corderman and Beauchamp[58] first reported ICR studies of the decarbonylation of acetaldehyde by $CpNi^+$ ($Cp=\eta^5$-$C_5H_5$). Interestingly, this species was unreactive with acetone and formaldehyde. In 1981 Freiser and coworkers used ICR

techniques to examine the reactions of $Cu^+$ and $Fe^+$ with ketones, ethers and aldehydes.[18-19] While copper ions either dehydrate ketones or cleave them into an enol (or ketone) and alkene, $Fe^+$ provides a richer variety of products. These include dehydrogenation and decarbonylation processes, along with generation of alkenes, alkanes, and smaller ketones. Schwartz et al.[23] studied the ligand enhanced selectivity in the C-H and C-C bond activation of ketones by $Fe^+$. In 1984 Beauchamp et al.,[13] using collision induced dissociation (CID), reported the chemistry of $Co^+$ with a variety of labeled aldehydes and ketones. They measured cross sections of the $Co^+ + (CH_3)_2CO$ reaction, reporting the exothermic production of $C_2H_6$ and CO + corresponding cations. Bowers and coworker[34] measured kinetic energy release distributions (KERDs) for loss of CO and of $C_2D_6$ from long lived $Co^+OC(CD_3)_2$ complexes. Based on semiquantitative arguments involving bond energies, Bowers and coworkers suggested that the rate limiting transition state involves insertion of $Co^+$ into the C-C bond of acetone. Additionally, density functional theory (DFT) has been applied to the $Ni^+$ assisted decomposition of acetone.[49] According to these DFT calculations, the rate limiting step is a $CH_3$ shift rather than C-C σ-bond activation.

*Electronic State Effects*

The ability of transition metal ions to activate the C-H and C-C bonds of hydrocarbons has been attributed to the high density of low-lying excited states available to the transition metal center.[62] However, the details of the interaction of these metals states with the reactant molecule are not well understood. Thus, the desire to understand these details has stimulated significant experimental and theoretical interest. Both theory and experiment indicate that the reactivity of any given state of the metal ion will depend

on its interaction with other nearby electronic states. Surface crossings are commonplace and "spin forbidden" reactions are often observed for transition metal ions. Spin is generally conserved for bimolecular reactions involving light elements, but only the total angular momentum must be rigorously conserved for heavier elements. Because reactions involving atomic transition metal ions are complex, quantitative state specific experimental studies along with theoretical calculations are necessary to understand such reaction dynamics and mechanisms.

Spin-forbidden reactions occur primarily for first row transition metals, because of large spin-orbital angular momentum coupling. Moreover the 3d orbitals are rather compact, rendering a small orbital overlap when binding to ligands.[11] The ground and low lying excited electronic configuration for the first row transition metal ions are either $3d^n$ or $4s3d^{n-1}$. The 4s and 3d orbitals are similar in energy giving rise to an abundance of low lying electronic states for first row transition metal ions.[62] Radiative lifetimes of many excited states of metal ions are long (on the order of seconds) owing to parity forbidden transitions. Consequently, once these long lived excited electronic states are produced, their reactivities can be studied. The electronic state configuration and corresponding energies for some first row transition metals ions is found in Table 1.

Our recent contributions to the study of organometallic ion chemistry in the gas phase has been the measurement of transition metal ions induced decomposition kinetics in ketones[63-66] and aldehydes.[67] Instrumentation has been developed that directly measures the rate constants associated with the gaseous metal ion/organic molecule reactions. Details about the instrument and its components as well as its operation are discussed in this dissertation. These studies have provided the rate constant for the rate limiting step along the coordinate that connects reactants to products. Furthermore, these

studies have suggested or quantified the energy of activation necessary to cleave organic σ-bonds resulting from this organic/transition metal cation interaction. Chapters three and four of this dissertation focus on measurements of decomposition rate constants of $h_6$ and $d_6$- acetone assisted by $Ni^+$ and $Co^+$. Rate constants were obtained over ranges of internal energies. Our results agree with earlier works in that each ion reacts with acetone in unique fashion. Arguments based on the electronic structure of each ion are made to explain such unique behavior. Chapter five presents preliminary results of our study of the reaction between $Ni^+$ and a cyclopentanone molecule. This represents the first ring-opening reaction investigated in our lab.

Table 1. Electronic states of $Fe^+$, $Co^+$ and $Ni^+$.

| Ion | State[a] | Configuration[a] | Energy ($cm^{-1}$)[a] |
|---|---|---|---|
| $Fe^+$ | $^4P$ | $3d^7$ | 13474.411 |
| | $^4D$ | $3d^64s(^5D)$ | 7955.299 |
| | $^4F$ | $3d^7$ | 1872.567 |
| | $^6D$ | $3d^64s(^6D)$ | 0 |
| $Co^+$ | $^3P$ | $3d^8$ | 13260.77 |
| | $^1D$ | $3d^8$ | 11651.48 |
| | $^3F$ | $3d^74s(^4F)$ | 9812.96 |
| | $^5F$ | $3d^74s(^4F)$ | 3350.58 |
| | $^3F$ | $3d^8$ | 0 |
| $Ni^+$ | $^2D$ | $3d^84s(^1D)$ | 23796.18 |
| | $^2F$ | $3d^84s(^3F)$ | 13550.39 |
| | $^4F$ | $3d^84s(^3F)$ | 8393.90 |
| | $^2D$ | $3d^9$ | 0 |

[a]Ref. 68

# CHAPTER TWO

## Experimental Apparatus and Technique

### *General Overview*

In general, the instrument consists of two vacuum chambers separated by a pneumatic gate valve. The expansion chamber is where the molecular beam is produced through a pulsed supersonic expansion. The base pressure in this chamber is $2*10^{-7}$ torr which is measured by an ionization vacuum gauge (KJL G-100KQF25). This chamber contains the ion source which is a stainless steel block connected to a Parker-Hannifin General Series 99 pulsed valve. The second chamber is a time-of-flight mass spectrometer (TOF-MS) with a base pressure equal to $1*10^{-8}$ torr. This TOF-MS contains two different sections: an acceleration region and a detection area separated by a 1.5 m tube. The accelerator is a grid of 7 parallel plates (Wiley-McLaren style arrangement)[69] and is used to repel the ions through the 1.8 meters of field free flight. The second region contains a custom-built hemispherical kinetic energy analyzer which is attached to a Chevron microchannel plate detector (Burle Industries). The hemispherical sector is used as an energy filter since the potential difference between the two hemispheres will only permit those ions that possess a certain kinetic energy to pass. Ions with different kinetic energies will have different transmission voltages.

Three diffusion pumps evacuate the instrument. A diffusion pump is located at each of the junctions of the molecular beam apparatus: the expansion chamber, the acceleration region, and the detection region. Each diffusion pump is backed by a mechanical pump. Liquid nitrogen traps separate each of the diffusion pumps from the

TOF-MS. These traps act as thermal barriers preventing diffusion pump oil from coating and damaging the electronics in the acceleration and detector regions. Although different kinds of experiments can be performed with this instrument, this chapter focuses on the description of the components necessary for both kinetic and dynamic studies.

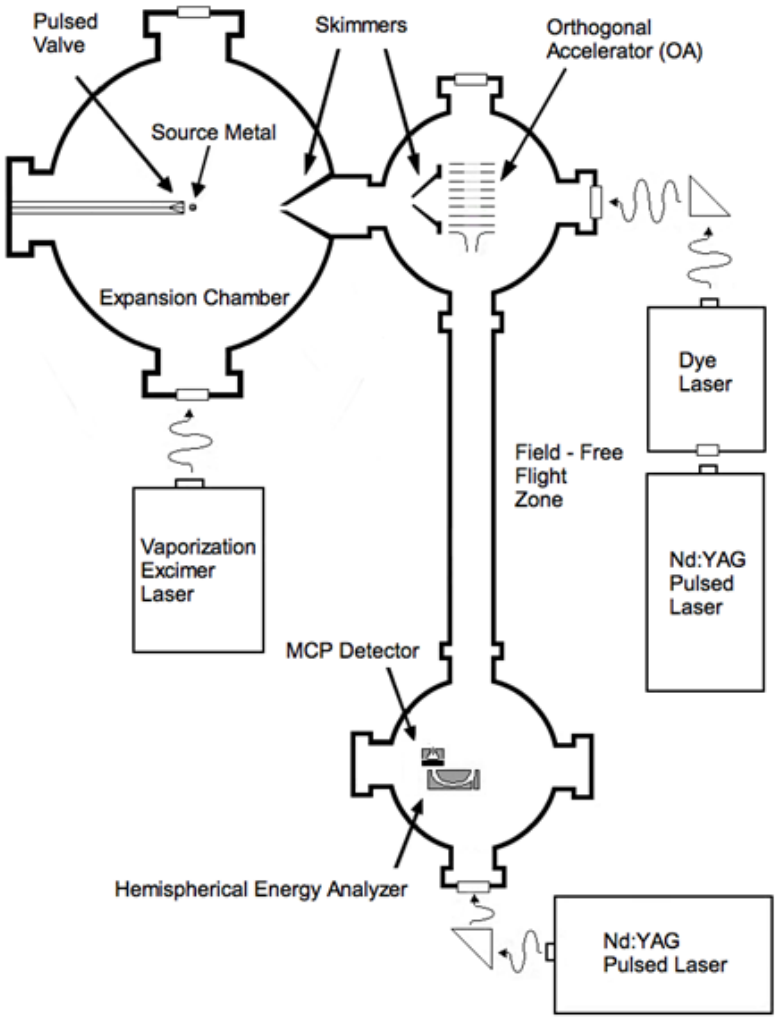


Figure 1. Diagram of the custom apparatus. Laser radiation can enter the vacuum apparatus through different viewports.

*Expansion Chamber*

The precursor cluster ions are generated in a jet cooled expansion in a 120 L vacuum chamber. An external DC motor (Figure 2) couples motion into the vacuum chamber and rotates a 5 mm transition metal rod at a rate of 1.1 rpm. This provides a relatively fresh metal surface for laser vaporization; additionally, this prevents localized over-heating in a single spot on the sample rod. The rotational motion is defined by high precision bearing rings press fit into an open configuration stainless steel source block. A high pressure line is coupled into the vacuum chamber that connects to the source block through a Series 99 General Valve. The valve/rod assembly is centrally located in this main vacuum chamber. Momentarily opening the solenoid valve allows a high-pressure carrier gas, doped with the organic vapor, to supersonically expand into the vacuum chamber.

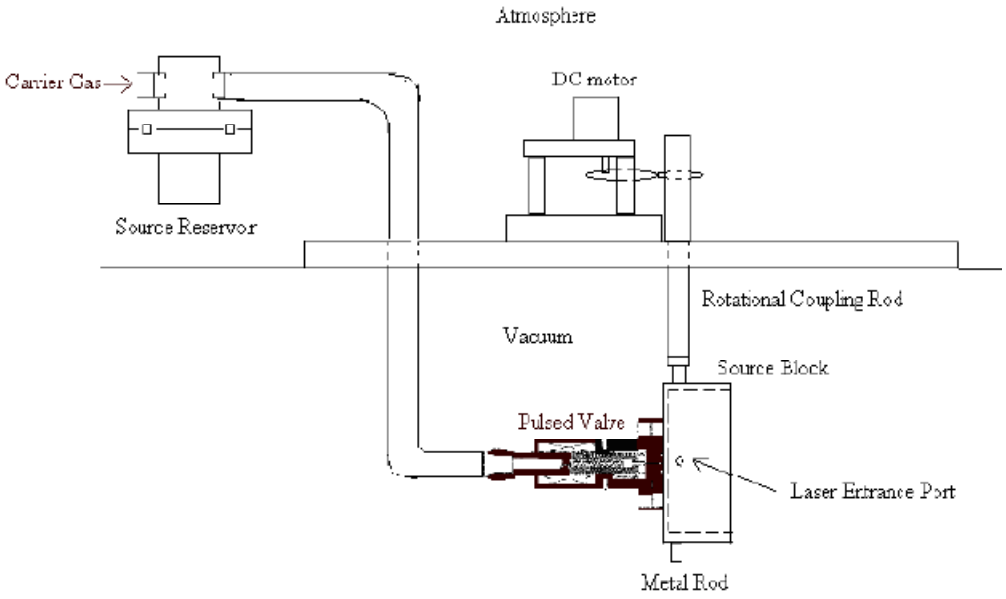


Figure 2. Inlet system for doped expansion gas (side view).

Radiation from the vaporization laser (excimer) is used to ablate the metal rod at the throat of the supersonic expansion. As the expansion plume develops, 248 nm laser radiation from a pulsed KrF excimer is focused through a quartz window and onto the rotating metal rod, thus ablating the metallic surface and seeding both neutral and ionic metal atoms into the expansion. The substantial number of collisions between the doped carrier gas and atomic metal cations ensures the formation of the clusters.

The pulsed valve used is a 316 stainless steel Parker Series 99 General Valve with a Kel-F® poppet. A schematic of the pulse valve can be seen in Figure 3. A driving pulse is applied to the coil assembly of the pulsed valve that magnetizes and compresses the main spring and pulls back the poppet. When this occurs, the expansion gas passes through the 1 mm nozzle orifice and into the expansion chamber. When the driving pulse has ended, the main return spring pushes the poppet back into the nozzle orifice, thus sealing the opening.

A critical parameter in this technique is the gas flow through the valve. This is controlled by the distance that the main spring is compressed. Shims are used to vary this distance. The shim width has a direct impact on the performance of the pulsed valve and varies per pulsed valve as well as with poppet condition.

Pulse valve voltage, pulse width, and shim distance are optimized prior to installation. Optimization of the pulse valve includes finding the shim width that permits gas flow rates of 10-20 ml/min. To seed the organic compound into the supersonic expansion, the carrier gas passes over the organic liquid contained in an external reservoir at room temperature (Figure 2). Thus, the organic vapor pressure of the organic is entrained in the carrier gas. The pulse valve is affixed by four equally spaced 10-32 bolts onto the sample source block. This source block is custom designed with dimensions

63.5 x 31.75 x 15.25 mm and is fabricated from 306 stainless steel. (See appendix for a detailed design of the source block).

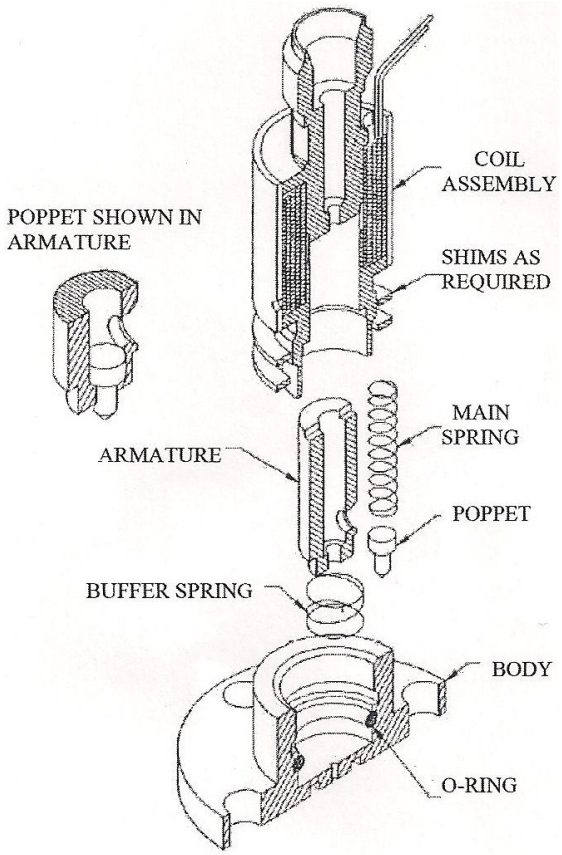


Figure 3. Schematic of a Parker Hannafin series 99 pulsed valve.

Figure 4 schematically shows a cross section of our custom-built source block. Carrier gas doped with the organic flows through a cylindrical channel with radius and length of 0.80 and 6.35 mm, respectively. The entrance to this channel is in line with the nozzle orifice of the pulsed valve. The length of this channel is minimized to ensure that the highest density of organic doped carrier gas interacts with ions formed through laser vaporization. The source block does not contain a growth channel, thus avoiding the production of large clusters. An O-Ring seal is located between the pulsed valve and the source.

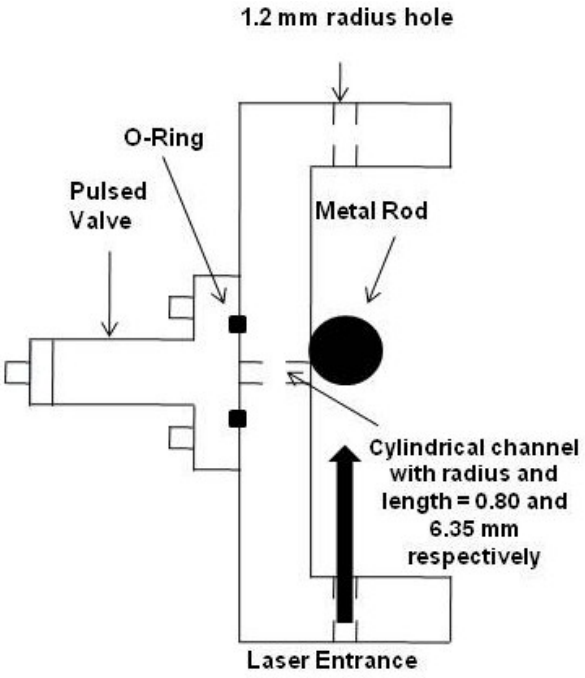


Figure 4. Cross section of source block used in our research. Excimer laser radiation is focused onto the metal rod through a 1.2 mm radius hole. Carrier gas doped with the organic vapor flows from the pulsed valve through a 0.80 mm radius and 6.35 mm length cylindrical channel. Organic molecules react with the metal plasma forming clusters.

The transition metal rod rotates freely within the source block. It is located ~3.25 mm from the block's center. The vaporization laser is timed to ablate the metal rod at the densest portion of the expansion. The two ~1.2 mm radius concentric holes are used to align the vaporization laser. The focused laser radiation is guided through these two holes while the instrument is at atmospheric pressure. The position of the laser focus is finely tuned by translating a 500 mm focal length positive lens located outside the vacuum chamber. This optimization is visually made by imaging the laser light onto a white screen placed approximately 2 m from the source. Optimization is realized when the highest most homogenous pattern is displayed on the screen.

The pulsed expansion gas is collimated twice prior to entering the TOF-MS chamber, forming a molecular beam. Thus, only the coldest, center portion of the

molecular beam is sampled. The molecular beam travels approximately 80 cm to reach the center of the acceleration region.

Two custom-built conical collimators skim the expanding beam. The cone angle of the first collimator is 30 degrees with a clear aperture of 8.5 mm. The length from the tip to the base is 15 cm. This collimator is located ~50 cm away from the pulsed valve. The second collimator also has a cone angle of 30 degrees but contains a smaller clear aperture with diameter equal to 5 mm. This is located ~75 cm away from the pulsed valve. The length from the tip to the base opening is 10 cm. Both collimators are constructed from aluminum metal.

*Time-of-Flight Mass Spectrometer (TOF-MS) Chamber*

The collimated molecular beam enters the center of the orthogonal accelerator (OA) which is located at the entrance of the TOF-MS (Figure 1). The design of the pulsed acceleration grid is based on the Wiley-McLaren[69] arrangement containing seven stainless steel square plates, each measuring 5 inches in each dimension. The OA repels the cationic species from the molecular beam and directs them through the TOF, where the common kinetic energy imparted to the ions permits mass separation by their m/z ratio. The positive voltage is provided by a Spellman SL 150 power supply. The acceleration grid is pulsed to high voltage after the molecular beam enters the grid.

Each OA plate has a 1 by 3 inch centrally located slot in the center of the plate. Each plate is stacked onto four 1 centimeter Teflon® spacers and supported by stainless steel all-threads. Each of the first five plates is electrically connected by 3 kΩ resistors. The final two plates are pressed together such that an O-Ring holds a thin nickel mesh, sandwiched between these two plates. The mesh is electroformed by Precision Eforming

to be exactly 70 wires per inch and permit 90 % maximum transmittance. This mesh establishes a uniform electric field between the final two plates of the acceleration grid. Mesh was placed in the through orifices of these two plates since the largest potential drop occurs here in accord with the Willey-McLaren design.[69]

The adiabatic expansion of the plume into vacuum establishes a small velocity component onto the ions. To compensate for this, a voltage controlled horizontal deflector was designed and placed at the OA exit. Variable voltage corrects for the horizontal velocity component. This repositions the ions toward the TOF center in line with the horizontal sector entrance.

The acceleration and detection regions are connected by a 1.5 meter length flight tube with an approximate inside diameter of 15 cm. The separated ion packet approaches a hemispherical kinetic energy analyzer which is located at the end of this field free region. The potential difference applied across the two sections of this device determines the ions that can pass to strike the detector.

The custom-built kinetic energy analyzer is fabricated from 316 stainless steel. The schematic is shown in Figure 5. The analyzer consists of three major components: outer and inner hemispheres, and a mounting plate. The outside and inside sections are maintained at a positive and negative potential respectively, while the mounting plate is electrically grounded. The potential difference across the sections of the sector can be selected to transmit the full kinetic energy of the ion beam, thus transmitting the different ions produced in the expansion. The variation in potential settings acts as an energy filter. Ruby beads and spacers electrically isolate the two halves. The hemispherical sector contains a channel through the outer hemisphere, permitting transmission of laser light along the TOF axis.

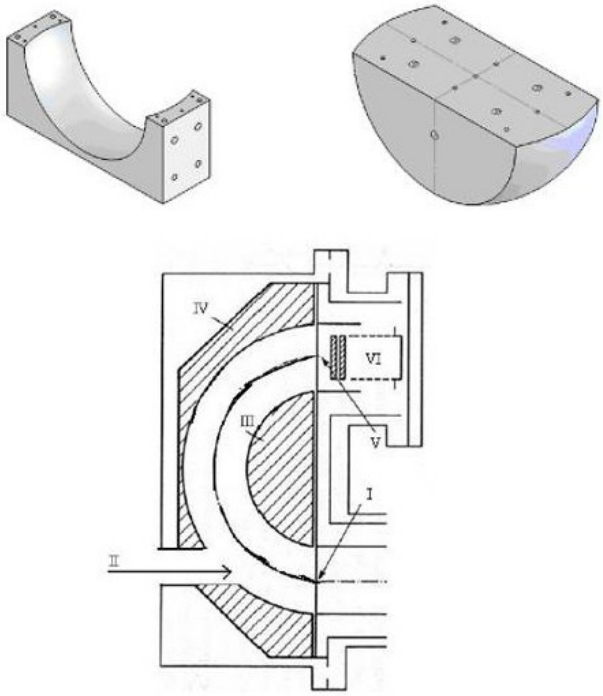


Figure 5. Schematic of the custom-built kinetic energy analyzer. Left top: Inner section of sector. Rigth top: Outer section of sector. Bottom: Aerial view. I) Ion beam entrance, II) Laser beam entrance, III) Inner section of sector, IV) Outer section of sector, V) Ion beam exit, VI) MCP detector.

As mentioned above, the ions have an associated kinetic energy due to their motion. This energy is related to the particle's mass and velocity. The energy is gained by the particle due to its interaction with the OA. This interaction accelerates the ion down the flight axis of the TOF-MS. By scanning the hemisphere potential, a full spectrum transmission voltage can be found. Figure 6 shows two sector voltage scans. Panel A displays the intensity of fragments that transmit the sector at various potential difference settings. The fragments are formed following laser photon absorption by the $Co^{+}$-Acetone cluster. Panel B shows the same type of results but the laser frequency was increased and the interaction location changed. As the potential difference is scanned,

only certain fragments transmit the sector and are detected. Each peak corresponds to a different fragment as is labeled.

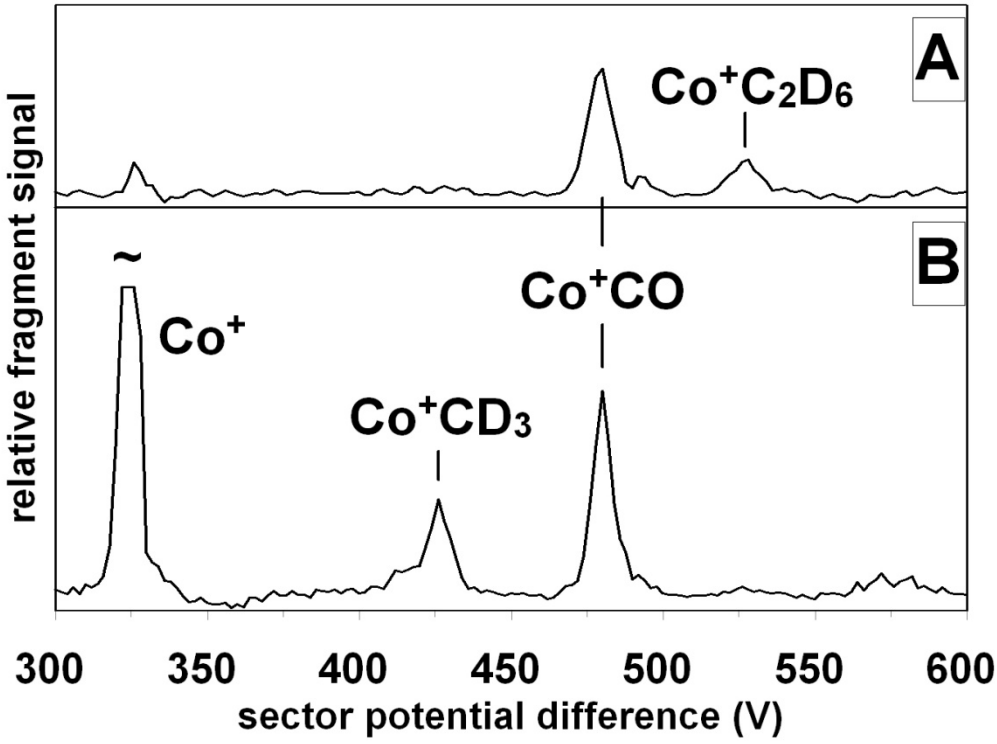


Figure 6. Sector voltage scans. Panel A: fragment ions resulting from the photon initiated, $Co^+$ assisted, reactive decay of acetone at an excitation energy=15900 $cm^{-1}$. Panel B: fragment ions resulting from high fluence photolysis of the $Co^+$Acetone isomers at a laser energy = 28200 $cm^{-1}$.

Although the dissociative event does not significantly impact the ion's velocity, the mass change alters the kinetic energy of the charged dissociated fragment. The optimal fragment transmission voltage across the halves of the sector is determined through application of eq 2.1:

$$\frac{m_f}{m_p} x V_p = V_f \tag{2.1}$$

where $m_f$ and $m_p$ are the mass of the fragment ion and precursor complex, respectively. $V_p$ is the full spectrum transmission voltage and $V_f$ is the sector pass voltage for that

fragment. Application of eq 2.1 determined the identity of the fragment ions labeled in Figure 6.

A Burle Industries, Inc. ChevronTM Model 3018MA MCP detector is located at the exit aperture of the hemispherical kinetic energy analyzer (Figure 5). The microchannel plate detector operates in a similar manner as continuous-dynode electron multipliers. When an ion strikes the top plate, it impinges upon a microchannel where electrons are liberated from the walls of the channel. The electrons that exit the first plate start a cascade on the next plate. The microchannels in the plates are oriented at an angle from each other in the Chevron style, thus inhibiting ion feedback and enhancing gain. The front plate of the MCP detector is operated at a constant -1.8 kV, while the back plate of the detector is held at a constant -100 V. Signal intensity is amplified 200 times by a fast Ortec-pre-amplifier, and the signal produced is 50 Ω terminated at the input to the data acquisition computer.

A Nd:YAG (Spectra Physics, Quanta Ray) that pumps a dye laser (Sirah) provides the laser radiation used in these studies. The Nd:YAG generates approximately 1000 mJ/pulse of 1064 nm light. The fundamental harmonic of the Nd:YAG is frequency doubled (532 nm) or tripled (355 nm) to either pump the tunable dye laser or to be used directly in the photodissociation studies.

*Photolysis, Kinetic and Dynamic Studies*

The apparatus has been designed to admit laser radiation through different ports. Thus, the photodissociation laser can intercept the molecular beam in different ways dictating the type of experiment that is performed. Two types of experiments are conducted here: photolysis and reactive decay. Photolysis experiments are performed by

directing laser radiation along the TOF axis. The light passes through the hole in the hemispherical sector (Figure 5), overlapping the counter-propagating ion beam just as the ions reach the sector entrance. UV and visible photolysis are used as preliminary experiments to identify possible fragment ions and to suggest likely precursor geometries. These photolysis events are fast and occur within the 1 μs travel time to the sector entrance. Fragments formed within the sector are not transmitted to the detector.

In order to measure the slow unimolecular decay of a precursor ion, cations within the molecular beam must absorb the photon energy prior to right angle extraction and mass separation within the TOF. This is accomplished by guiding the laser radiation through a viewport along the supersonic expansion axis. The laser radiation thus overlaps the counter propagating molecular beam. The precursor ions absorb radiation and the unimolecular decomposition is initiated, producing fragments ions as the molecular beam approaches the OA. All fragment ions produced in the expanse between the location of photon absorption and the OA receive the same kinetic energy imparted to the precursor ions during right angle extraction. These early fragment ions are indistinguishable from the precursor ions in the parent beam and are therefore not sampled. Only those precursor ions that decay within the field free flight region of the TOF can be detected by selective transmission through the sector.

An example of a typical waveform obtained by selectively sampling a fragment ion from precursor decay is shown in Figure 7. Here the precursor ion, $Ni^+$-Acetone, absorbs 18000 $cm^{-1}$ ($\lambda$ = 555 nm) of photon energy and is dissociated into $Ni^+CO$ and $C_2H_6$.[65] As the precursor cluster ions are jet cooled in the supersonic expansion, the photon energy represents the amount of internal energy available to the complex. The time axis indicates when the pulsed laser is triggered to fire with respect to the ion's

temporal displacement relative to the OA. This is most conveniently defined as negative quantities. The top panel of Figure 7 plots the natural logarithm of the integrated intensity as a function of time. The linear portion is fit to a straight line and the rate constant extracted from linear regression analysis. This value is presented in the figure.

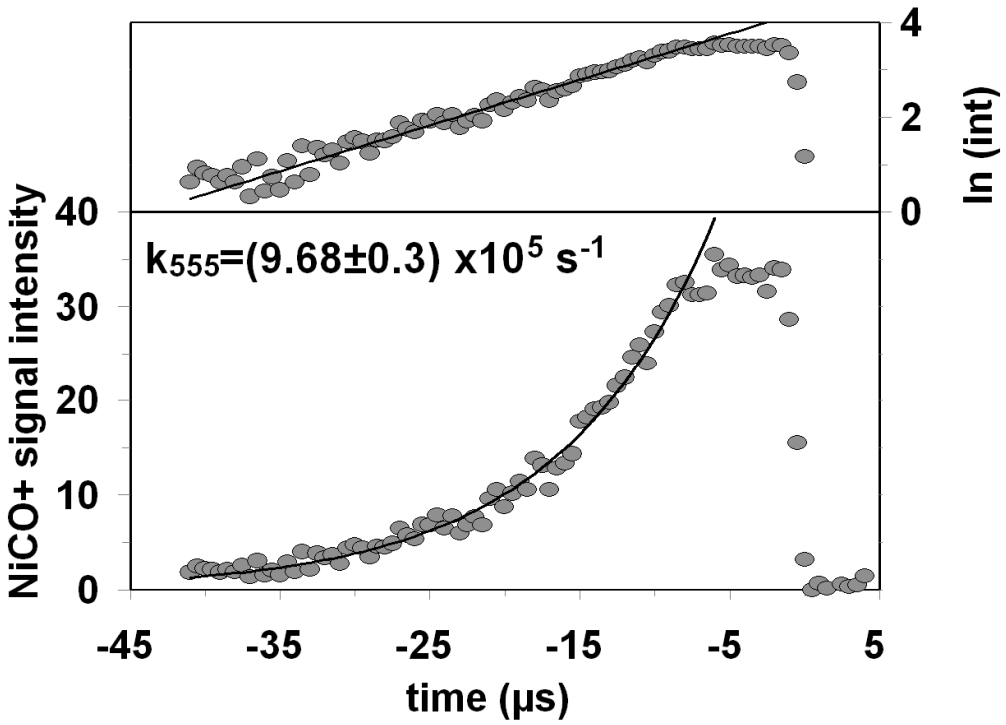


Figure 7. Typical product growth waveform resulting from nickel cation assisted decomposition of acetone upon absorption of 18000 $cm^{-1}$ of photon energy (bottom panel). Top panel plots the natural logarithm of the intensity vs. time, and then the first order rate constant is extracted.

The remainder of this dissertation focuses on the photon-induced, metal ion assisted decomposition of $Ni^+$-acetone and $Co^+$-acetone systems. Additionally, preliminary results for the decomposition of cyclopentanone assisted by nickel cation are presented. This final study in my career here represents the first ring opening reaction studied by these methods.

# CHAPTER THREE

## Unimolecular Decomposition of $Ni^+$-Acetone and its Rate Limiting Step

This chapter reproduced in part with permission from:

- Castleberry, V.A.; Dee, S. J.; Villarroel, O. J.; Laboren, I. E.; Frey, S.E.; Bellert, D. J. *J. Phys. Chem. A* **2009**, *113*, 10417.
- Dee, S. J.; Castleberry, V. A.; Villarroel, O. J.; Laboren, I. E.; Frey, S. E.; Ashley, D.; Bellert, D. J. *J. Phys. Chem. A* **2009**, *113*, 14074.

### *Introduction*

It is well known that C-C and C-H bonds in hydrocarbons can be activated by transition metal ions in the gas phase.[1-11] They can interact with organic molecules aggressively to cleave rather high energy bonds, essentially catalyzing organometallic reactions.[12-47] The energy lowering associated with metal-mediated, organic bond activation is of obvious importance. Detailed understanding of the energy requirements, dynamics, and mechanisms of organic bond cleavage reactions assisted by transition metals is of practical significance to diverse fields such as enzymology and to those industries researching and developing alternative energy sources.

The body of literature associated with gas phase ion/molecule reactions is extensive and diverse. Decomposition reactions of alkanes, alkenes, ethers, ketones, and aldehydes with metals ions such as $Ni^+$, $Cu^+$, $Fe^+$, and $Co^+$ have been studied both experimentally and theoretically. The results presented here builds upon this knowledge base through the direct experimental determination of ion/molecule reactions kinetics.[65-66]

Freiser and coworkers[19] have used the ion cyclotron resonance (ICR) technique to study the reaction of $Fe^+$ with $(CD_3)_2CO$. They found the neutral product yield to be 93%

$C_2D_6$ and 7% CO. Beauchamp and co-workers[13] measured the collision induce dissociation (CID) cross sections of the $Co^+ + (CH_3)_2CO$ reaction. This established a similar neutral product distribution of $C_2H_6$ (90% yield) and CO (10% yield).

More recently, product kinetic energy release distributions (KERDs) for $Co^+$, $Ni^+$, and $Fe^+$ reacting with acetone have been measured.[34] Bowers et al. measured the KERD for the $NiCO^+$ product ion from the decomposition of $Ni^+(CH_3)_2CO$. Their analysis indicated that C-C σ-bond activation was the rate limiting step in this decomposition reaction

In addition to the experimental studies of ion/acetone reactions, density functional theory (DFT) has been applied to the decomposition of $Ni^+(Ac)$ into $Ni^+CO + C_2H_6$.[49] The reaction potential energy surface has been calculated and Figure 8 is a simplified version of this mechanism. It begins with the encounter complex (*EC*) which is the $Ni^+$ cation bound to the dipole of the neutral acetone molecule. The $Ni^+$ inserted complex is the first intermediate ($I_1$) in the mechanism. This forms once the EC receives sufficient energy to overcome an activation barrier. The transition state structure ($TS_1$) shows the cation approaching the C-C s-bond. Formation of TS1 is controlled by the bond activation rate constant ($k_{act}$). Formation of the second intermediate ($I_2$) occurs as $I_1$ traverses the second transition state ($TS_2$). This structure shows three bonds to the $Ni^+$ cation and is formed as the methyl group shifts to the $Ni^+$ center forming the tri-coordinate cation. This process is governed by the rate constant $k_{sft}$. The final step breaks the electrostatic bond of $I_2$ forming $Ni^+CO$ and $C_2H_6$. This final step has no kinetic barrier and thus the value of this final rate constant ($k_3$) is likely relatively large. According to DFT calculations, the energy of *TS2* is greater than *TS1*, indicating that the rate limiting step is the $CH_3$ migration rather than C-C σ-bond activation.

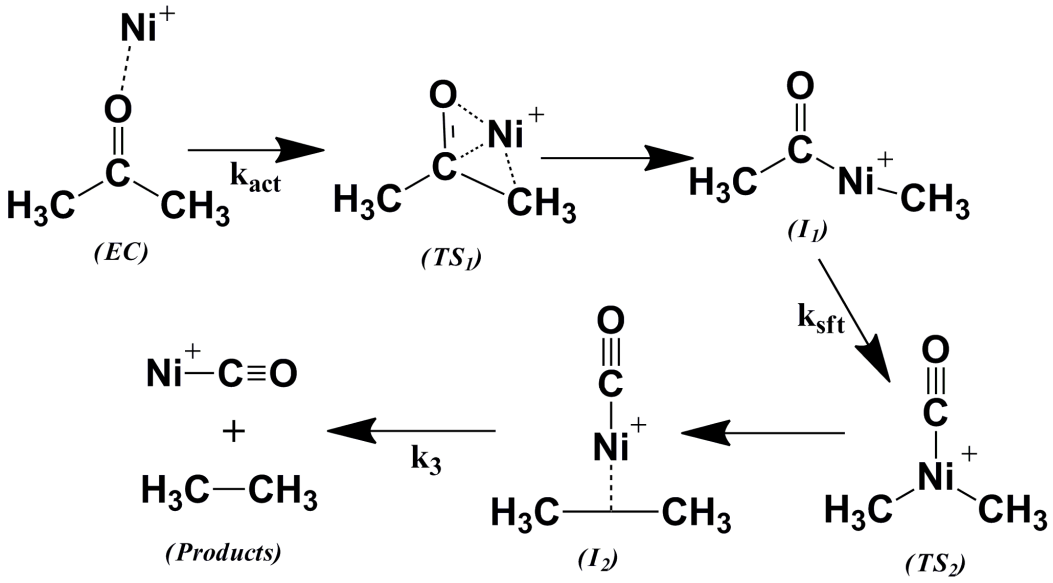


Figure 8. Proposed mechanism for the $Ni^+$-assisted decomposition of acetone.

As indicated, our contribution to this area of science is the determination of unimolecular decomposition reaction rate constants. Unique to our technique, is the formation of cold precursor ions, through supersonic expansion. Thus, the ions are formed with minimal amounts of internal energy. The activation energy is supplied to the EC through absorption of a laser photon. Unimolecular decomposition of the precursor ion occurs and the excited system develops in time according to:

$$A_t = A_0 e^{-kt} \tag{3.1}$$

This chapter briefly presents and discusses the measurements of rate constants for the low energy $Ni^+$ assisted decomposition of gaseous acetone under jet cooled conditions. The energies used to initiate the reaction of the precursor ions, $Ni^+(h_6\text{-Ac})$ and $Ni^+(d_6\text{-Ac})$, are well below that required to cleave C-C σ-bonds in the isolated acetone molecule. The rate limiting step was assigned by comparing the decomposition rate constants of these two complexes. Arguments are made suggesting that $CH_3$ migration ($k_{sft}$, Figure 8) is the rate limiting step in the dissociative reaction. The $Ni^+(Ac)$

precursor concentration decreases in time according to eq 3.1. The formation of $Ni^+CO$ fragment ion is selectively monitored. The rate constant $k$ is then extracted and represents the rate limiting step (either formation of $TS_1$ or $TS_2$) along the reaction coordinate.

*Generation and Identification of $Ni^+(Ac)$ Precursor Ions*

$Ni^+(Ac)$ complexes are generated under jet cooled conditions by some methods described in chapter two. Briefly, the focused vaporization laser (12-15 mJ/pulse of 248 nm light) ablates the nickel rod (~98% pure) seeding neutral and charged nickel atoms into the jet cooled expansion. The nickel ions interact with the gaseous acetone carried by helium gas into the expanding beam. The substantial number of collisions between the doped carrier gas and $Ni^+$ ensures the formation of the $Ni^+(Ac)$ complex which, due to the large pressure drop between the static gas reservoir and the vacuum chamber, is formed with minimal amounts of internal energy.

The expanding plume is skimmed twice and enters a pulsed Wiley-McLaren[69] orthogonal accelerator (OA). A nearly 2 kV voltage pulse provides the common kinetic energy to the ions and accelerates them through the TOF. The ions are temporally and spatially separated as they reach the entrance aperture to a kinetic energy analyzer. Here a potential difference across the two halves of the sector (680 V) transmits the full kinetic energy of the ion beam. Thus, the different ionic species produced in the expansion travel through the sector to strike the MCP detector located at the sector's terminus. Figure 9 shows a typical mass spectrum obtained in this study. Precursor mass spectra are analyzed to determine the identity and optimize the intensity of the complexes within the beam. The 58 and 60 isotopes of the Ni are clearly discernable in Figure 9.

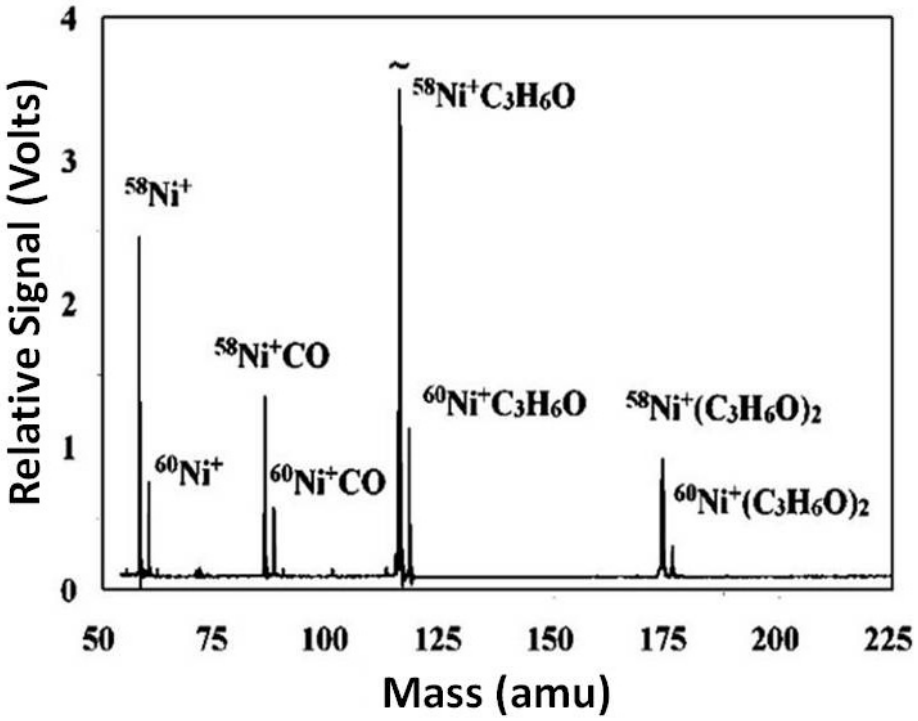


Figure 9. $Ni^+$(Ac) precursor time-of-flight mass spectrum.

Laser induced dissociation of a single precursor ion results in charged fragments that transmit through the sector at different characteristic voltage settings. Although the dissociation event does not significantly affect the fragment's velocity, the transmission voltage changes due to the change in mass of the fragment ion. Figure 10 shows such a fragment transmission profile resulting from the laser induced dissociation of the $Ni^+$(Ac) precursor cluster ion. Here, 16400 $cm^{-1}$ laser radiation is timed to intersect the $Ni^+$(Ac) precursor ion 6 μs before it enters the sector. The x-axis represents the potential difference between the inner and outer surfaces of the hemispherical kinetic energy analyzer. The precursor ion dissociates into three dissociative products which are observed in high yield are $Ni^+$, $Ni^+CO$, and $CH_3CO^+$. The shoulders observed in Figure 10 at ~365 V and ~535 V are due to the $^{60}Ni$ isotope of each cluster. The identities of the

ionic fragments are determined from the potential difference applied across the two sections of the kinetic energy analyzer according to the eq 2.1.

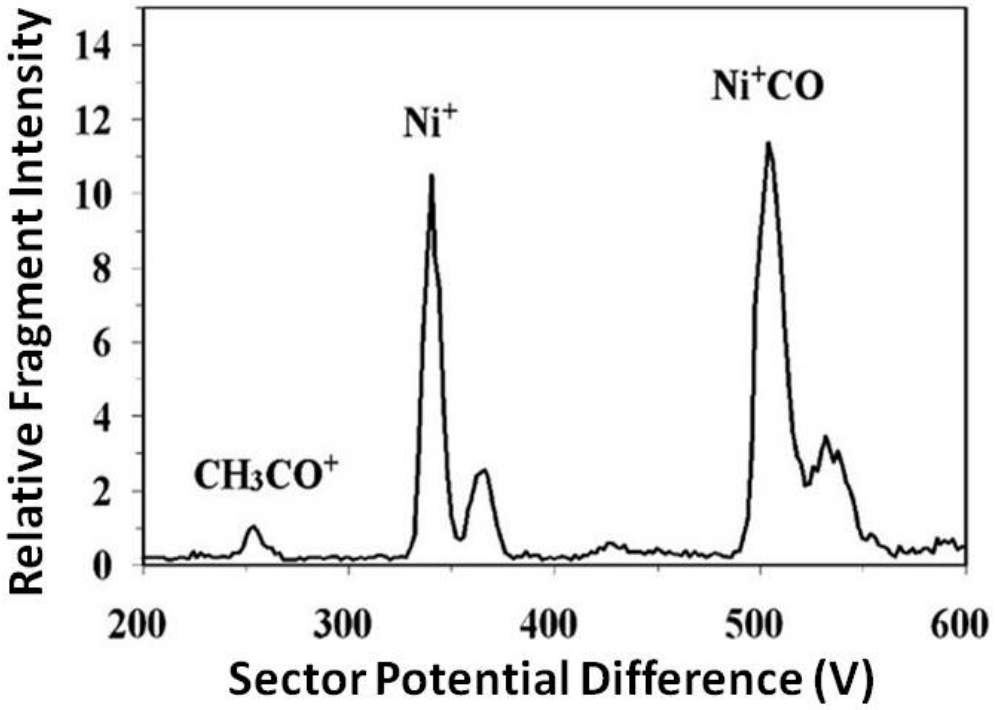


Figure 10. Sector voltage scan monitoring $Ni^+(Ac)$ dissociation. Laser radiation of 16400 $cm^{-1}$ is timed to intersect the molecular beam 6 μs before entrance into the sector. The identities of the fragments are indicated above each peak.

Photodissociation studies, in which a pulsed laser field intersects the ion beam just before the ions enter the sector, reveal the various types of fragment ions resulting from precursor dissociation. Such preliminary experiments indicate the identity of possible fragment ions; however, probing the ion beam inside the TOF proves incapable of measuring reaction rate constants. Rather, to measure the unimolecular decay of a precursor ion, cations within the molecular beam absorb the photon energy prior to right angle extraction and mass separation within the TOF. This is accomplished by guiding the laser beam into the vacuum apparatus to intersect the ion beam along the supersonic expansion axis. The ionic molecules within the beam absorb the radiation and decay

producing fragment ions as the molecular beam approaches the OA. All fragment ions produced in the expanse between photon absorption and the OA receive the same (full) kinetic energy imparted to the precursor ions during right angle extraction. These "early" fragment ions are indistinguishable from the precursor beam and are therefore not detected. Only those precursor ions which decay within the field free flight of the TOF can be detected through selective transmission through the sector. Hence, our sector limits detection to those dissociation events that occur during the precursor ion field free flight within the TOF. Waveforms are generated by a computer controlled scan of the timing delays. The program varies when the dissociation laser encounters the molecular beam while measuring the intensity of selected fragment transmission through the sector.

Selectively monitoring fragment production that occurs only during the free flight time between the OA and sector discriminates against the detection of any fast dissociative events. Ions require ~2.4 μs to traverse the OA at nominal voltage settings and any precursor which dissociates within the field of the OA will not be detected. Thus, fast 2-photon dissociation processes provide minimal contamination to the fragment yield even at the high, pulsed laser fluences (30-50 mJ/pulse) employed for these studies.

Of the three fragment ion products observed in Figure 10, only production of $Ni^+CO$ results from single photon absorption. This has been confirmed by conducting the analogous sector scan but where the laser intersects the molecular beam 3 μs prior to orthogonal extraction. This effectively discriminates against dissociation caused by multi-photon absorption (which must be a comparatively fast process). The lack of observed signal indicates that the cleavage channel (production of $Ni^+$) and the charge transfer dissociative channel (production of $CH_3CO^+$) are multi-photon induced events.

Additionally, the identity of the fragment $Ni^+CO$ has been confirmed through isotopic (deuterium) labeling of the acetone ligand.

*Electronic Transition and Energy Deposition*

The ground electronic state of the $Ni^+(Ac)$ complex ion is likely formed from the electrostatic attraction between the ground state $Ni^+$ cation $[3d^9(^2D)]$ and the neutral acetone dipole. The bonding is likely electrostatic as the ion-dipole attractive potential, at the $Ni^+$-$OC(CH_3)_2$ distance predicted by theory,[49] is 19600 $cm^{-1}$. The bond energy of $Ni^+(h_6\text{-Ac})$ has been calculated[49] as 20300 $cm^{-1}$. The energy required to ionize atomic nickel is ~16500 $cm^{-1}$, less than that required to ionize acetone.[72] This large difference in ionization energy suggests that the charge in the complex is localized on the nickel.

Upon laser radiation, the $Ni^+(Ac)$ cluster ion absorbs a visible photon and is promoted to an electronically excited state. The nickel cation is the chromophore, as the electronic transitions in acetone occur only in the UV.[73-74] The lowest lying, excited electronic state of $Ni^+$ is a $[3d^84s(^4F)]$ with lowest energy spin-orbit component (J=9/2) lying 8393.9 $cm^{-1}$ above the $Ni^+$ $^2D$ ground state (Table 1). Electronic transition into this $^4F$ manifold of states likely initiates the dissociative chemical reaction observed in this study. This $Ni^+$-centered electronic transition $[3d^84s(^4F)] \longleftarrow [3d^9(^2D)]$ is both spin and parity forbidden. The prepared, excited quartet electronic state of $Ni^+(Ac)$ is metastable; the absorbed photon energy is insufficient to cause direct dissociation into $Ni^+$ and acetone fragments, and coupling to the ground state through photon emission is optically forbidden. Rather, the excited quartet state intersystem crosses to the double electronic state and deposits the energy of the electronic transition into the high vibrational level of the ground state. Energy deposition in these high vibrational states provides the

activation energy for unimolecular dissociation into fragments. Additionally, the deposited photon energy is likely localized in the cluster vibrational modes (those involving motion between the $Ni^+$ and neutral acetone) of the molecule. The cluster modes may inefficiently couple to the vibrational modes of the acetone molecule. The net effect of this coupling is the localization of energy and provision of sufficient motion to allow $Ni^+$ activation into the C-C σ-bond in acetone.

*Data Analysis*

Molecular cations, upon absorption of the laser photon energy, will dissociate as indicated in the mechanism of Figure 8. Because unimolecular decomposition is a first order process, excited precursor ions will decay in accord with eq (3.1). Here, the precursor molecule absorbs radiation, initiating the reaction, before entering into the OA. Only the precursors which decompose after exiting the OA, but prior to entering the sector, will produce detectable fragment ions. So, the molecular decay is sampled during the entire field free flight through the TOFMS. This sampling method has the effect of integrating eq 3.1 between two well defined limits: $t_i$ = the time the precursor ions just exit the OA; and, $t_f$ = the time just prior to the precursor ions entering the sector. The integrated area is then plotted as a single point, $y_\tau$. The time $\tau$ represents the temporal displacement of the ions from the OA at the time of photoabsorption. This represents the decay that is lost (not sampled) during the ions flight to the OA. This is most conveniently defined as negative time values, and time = zero τ represents the coincident firing of the dye laser and OA. Thus, the only fragment signals lost are from those precursors which decay within the 2.4 μs travel through the OA field.

The signals acquired in this study result from integrating eq 3.1 between the limits $t_i$ and $t_f$

$$= A_0 \int_{t_i}^{t_f} e^{-kt}\, dt = \frac{A_0}{k}\left(e^{-kt_i} - e^{-k(\Delta t + t_i)}\right) = \frac{A_0}{k}\left((e^{-kt_i}\left(1 - \frac{1}{e^{k\Delta t}}\right)\right) \quad (3.2)$$

Grouping the constants of equation 3.2 into α:

$$\alpha = \frac{1-\frac{1}{e^{k\Delta t}}}{k} \quad (3.3)$$

and substituting $t_i = \tau + 2.4$ μs results in equation 3.4, which has the same form of equation 3.1.

$$y_\tau = \left(\frac{\alpha}{e^{2.4k}}\right) A_0 e^{-k\tau} \quad (3.4)$$

Thus, the unimolecular reaction rate constant can be extracted from a plot of $y_t$ vs τ. A benefit to this technique is that the TOF serves two purposes, it separates different precursor ions in time and it functions as a signal integrator in accord with eqs 3.2-3.4. Comparing eqs 3.1 and 3.4, both equations have the same exponential form; however, the pre-exponential factor is multiplied by the term in parentheses in eq 3.4. In fact, taking the ratio of eq 3.4 to eq 3.1 suggests that the signal acquired here ($y_t$) is amplified by this parenthetical term relative to the signal acquired without integration ($A_t$).

Figure 11 is a graphical representation of the enhanced signal associated with monitoring unimolecular decay with rate constant = $5 \times 10^4$ $s^{-1}$. The shaded portions of the three smaller graphs indicate the integrated areas from eq 3.2. They are plotted as three points in the lower graph. Under the conditions implied in Figure 11, the signal enhancement is 17.2 x. This amplification is the primary reason why decay following such low oscillator strength electronic transitions is observable by this technique.

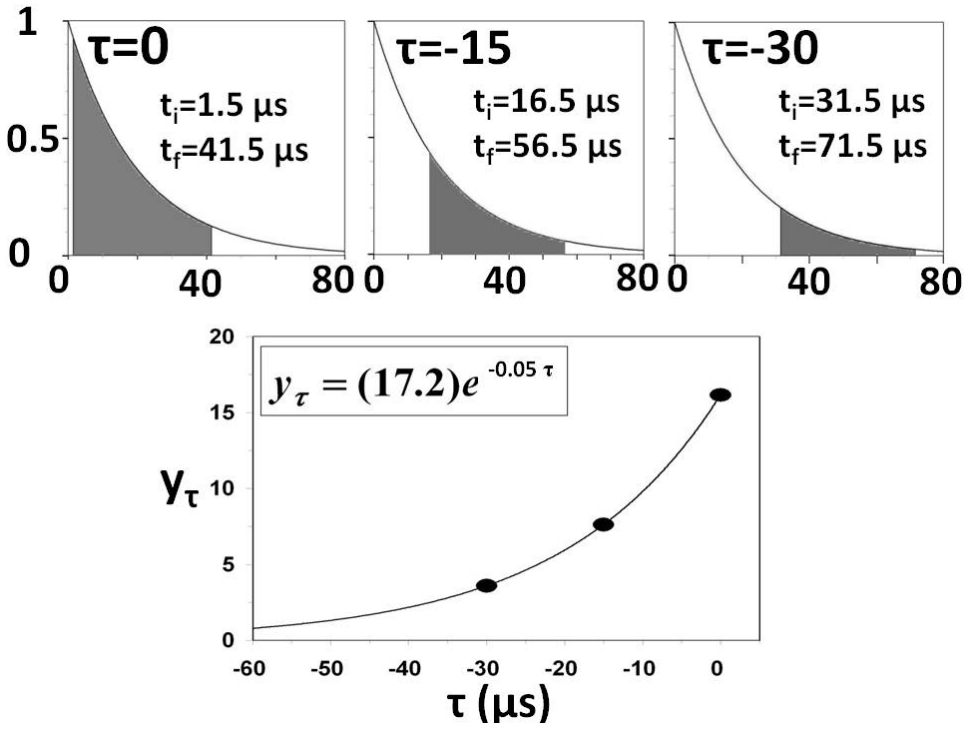


Figure 11. Signal amplification associated with this technique. The three smaller graphs plot the function $y=e^{-0.05\tau}$. The shaded portions represent the integrated areas that are plotted as three points in the lower graph.

## *Results*

### *Decomposition of $Ni^+(h_6$-Ac) Complexes*

The three panels of Figure 12 show the exponential decay profiles of $Ni^+$(Ac) dissociating into $Ni^+CO$ and $C_2H_6$, which directly result from absorption of the different photon energies. As the ionic complexes are jet cooled in the supersonic expansion, the photon energy approximates the internal energy available to the complex. The time axes of these panels indicate when the pulsed laser is triggered to fire with respect to the ion's temporal displacement relative to the OA. Zero time is defined to be the laser trigger timing at which the ions turn away from the laser beam and are pulsed accelerated out of the acceleration grid. At times later than 0 μs, the laser misses the ion beam and any

signal observed results from collision induced dissociation. At times earlier than 0 μs (negative number), the laser intersects the molecular beam and induces dissociation; the subset of which occurs within the TOFMS is selectively detected by the MCP detector.

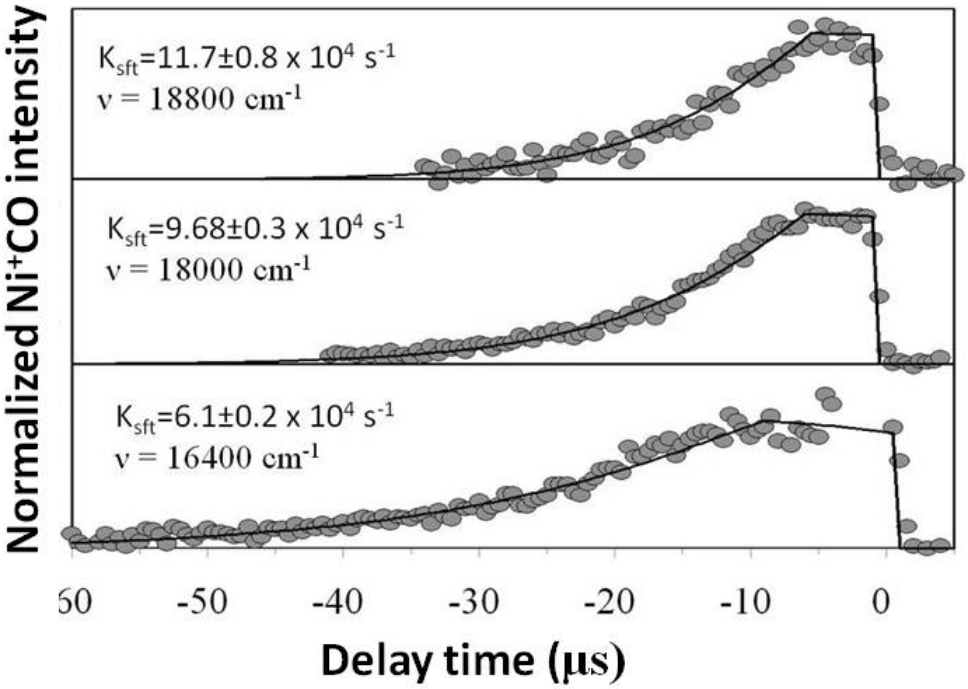


Figure 12. Waveforms acquired from the selective sampling of $Ni^+CO$ from the unimolecular decomposition of $Ni^+(Ac)$ precursor complex. The rate constants are extracted from the long exponential portion of the decay curve.

The unimolecular decay curves of Figure 12 show unique behavior. In each, the early data does not vary with time. The remaining data follow first-order decay only after this plateau. This time lag is an induction period and results from either the relatively slow production and buildup of an intermediate, or from the relatively slow consumption of the intermediate. The reaction rate constants provided in Figure 12 and Table 2 are acquired by plotting the natural logarithm of the waveform intensity versus time and extracting the slope from the linear portion of the waveform. These decay profiles suggest that there are two rate constants that mediate the kinetics of the reaction. One of

the rate constants is rate determining and the other is slightly larger. Both decrease with decreasing energy as can be observed in Table 2.

Table 2. Rate Constants ($x10^4$ $s^{-1}$) measured for the $Ni^+$ assisted decomposition of acetone at low energies. Rate constant subscript represents an action; methyl shift (sft) or bond activation (act). Rate constants without error are calculated though simulation

| Internal Energy ($cm^{-1}$) | $Ni^+(h_6$-Ac)[a] | | | $Ni^+(d_6$-Ac)[b] | | | $k_H/k_D$ | |
|---|---|---|---|---|---|---|---|---|
| | $k_{act}$ | $k_{sft}$ | $t_{ind}$(μs) | $k_{act}$ | $k_{sft}$ | $t_{ind}$(μs) | act | sft |
| 18800 | 22 | 11.7±0.8 | <1.5 | | | | | |
| 18000 | 20 | 9.68±0.3 | 10.4±1.0 | 12.5 | 1.60±0.08 | 18±4 | 1.6 | 6.1 |
| 17700 | 20 | 9.27±0.3 | 10.9±1.0 | | | | | |
| 16800 | | 6.33±0.3 | | | | | | |
| 16400 | 13 | 6.10±0.2 | 16.5±1.0 | 6.7 | 1.17±0.06 | 35±4 | 1.9 | 5.2 |
| 16100 | | 5.80±0.3 | 16.5±1.0 | | | | | |
| 15600 | | 5.60±0.3 | 17.5±1.0 | | | | | |

[a]Ref. 65. [b]Ref. 66

Based on the mechanism in Figure 8, the likely choice for these two rate constants are $k_{act}$ (the formation of $TS_1$) and $k_{sft}$ (the formation of tri-coordinated $Ni^+$, $TS_2$). The value of $k_3$ is assumed large as this involves the direct elimination of the electrostatically bound ethane molecule from $Ni^+CO$ without rearrangement. This assumption is consistent with DFT calculation of the potential energy surface. Figure 8 suggests a reaction coordinate of consecutive steps to produce $Ni^+CO + C_2H_6$ from the precursor $Ni^+$(Ac). Our results suggest that the reaction kinetics is controlled by the formation of two transition states, making both $k_{act}$ and $k_{sft}$ kinetically important steps along the reaction coordinate. The solutions to the differential rate equations that govern precursor loss and fragment production have been solved for this type of system by Harcourt and

Esson.[70-71] Following their treatment, the time variations in the concentrations of $(Ni^+Ac)_t$, the first intermediate in Figure 8 $(I_1)_t$, and product $(Ni^+CO)_t$ can be derived:

$$(Ni^+(Ac))_t = (Ni^+(Ac))_0 e^{k_{act}t} \quad (3.5)$$

$$(I_1)_t = \left(Ni^+(Ac)\right)_0 \frac{k_{act}}{k_{sft}-k_{act}} (e^{-k_{act}t} - e^{-k_{sft}t}) \quad (3.6)$$

$$(Ni^+CO)_t = \frac{(Ni^+(Ac))_0}{k_{sft}-k_{act}} \left[k_{sft}(1 - e^{-k_{act}t}) - k_{act}(1 - e^{-k_{sft}t})\right] \quad (3.7)$$

we define the difference in rate constants as $\Delta k = |k_{sft} - k_{act}|$. Under conditions when $\Delta k$ is large, eq 3.7 reduces to:

$$(Ni^+CO)_t = \left(Ni^+(Ac)\right)_0 (1 - e^{\kappa t}) \quad (3.8)$$

where $\kappa = k_{act}$ when activation of the C-C σ-bond is rate limiting ($k_{act} << k_{sft}$); and $\kappa = k_{sft}$ when isomerization (the metal mediated methide shift) is rate limiting ($k_{act} >> k_{sft}$). Regardless, under conditions when $\Delta k$ is large, the production of fragment $Ni^+CO$ occurs simultaneously as the precursor ($k_{act}$ rate limiting), or the intermediate ($k_{sft}$ rate limiting) decays. This results in sharp behavior in the early times of the decay profile. When Δk is small, a time lag between the initial decay of the precursor and the ultimate fragment formation may be observed. These induction times, which become more apparent as Δk approaches zero, are responsible for the time independent features in Figures 12.

*Decomposition of $Ni^+(d_6$-Ac) Complexes and Determination of the Rate Limiting Step.*

The results obtained in the decomposition of acetone assisted by $Ni^+$ and presented in the previous section indicate that either formation of $TS_1$ and subsequent C-C σ-bond activation is the rate limiting step or the cation-mediated methyl migration is rate limiting. To determine whether $k_{act}$ or $k_{sft}$ is smallest, unimolecular decomposition of

the deuterium labeled $Ni^+(d_6\text{-Ac})$ is monitored and compared with the previous $Ni^+(h_6\text{-Ac})$ system (Figure 8).

The bottom panel of Figure 13 shows the waveform obtained from the decomposition of the $Ni^+(d_6\text{-Ac})$ precursor into $Ni^+CO$ and $C_2D_6$ resulting from the absorption of 16400 $cm^{-1}$ of laser radiation. The top panel of reproduces the $Ni^+$-assisted decay of $Ni^+(h_6\text{-Ac})$. Both waveforms were acquired at the same laser energy (16400 $cm^{-1}$) and comparable instrumental settings. Figure 13 shows obvious differences between these measurements. The rate constant extracted in the low energy activation of acetone by gaseous $Ni^+$, is ~5 times smaller for the heavier, deuterium labeled acetone isotope at the reaction initiation energy used in this study. To validate this result, analogous measurements are conducted using other laser energies and is provided in Table 2.

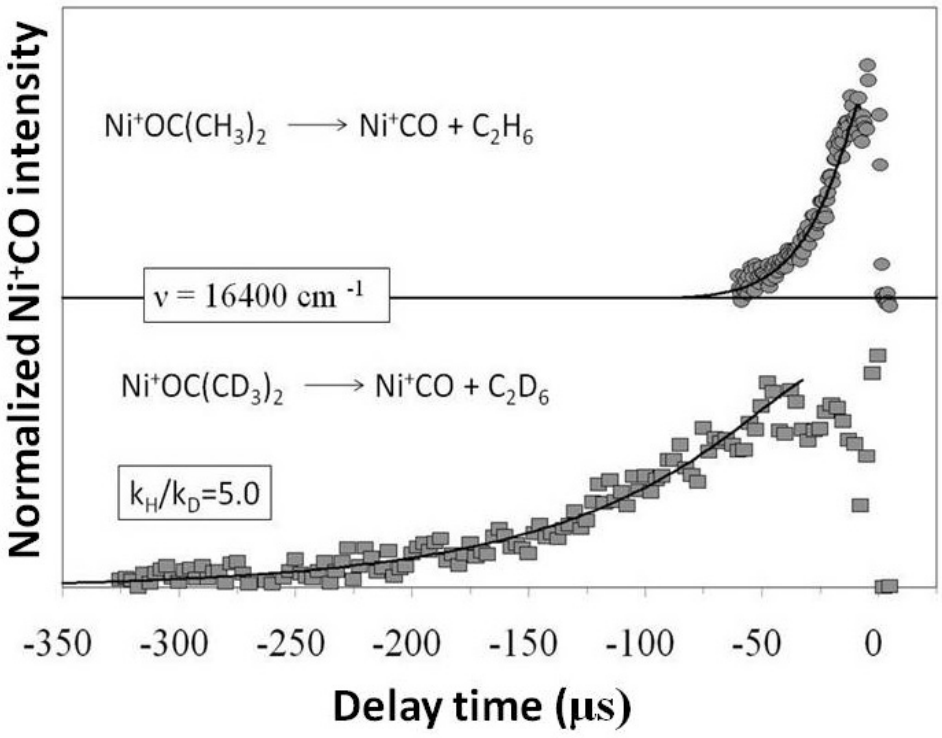


Figure 13. Comparison between the decomposition of $Ni^+(h_6\text{-(Ac)})$ (top panel) and $Ni^+(d_6\text{-(Ac)})$ resulting from the absorption of laser radiation with energy = 16400 $cm^{-1}$.

The large ratio magnitude observed suggests that there must be significant motion of the isotopically labeled methide during the formation of the rate limiting transition state. The logical candidates for the rate limiting step are either the formation of TS1 or $TS_2$. The formation of both transition states have been implicated as the rate limiting step in the mechanism. It is clear that the rearrangement to form $TS_2$ involves significant motion of the methyl group and therefore this must be the rate limiting step. This conclusion is supported by recent DFT calculations.[49]

*Waveform Simulations*

As indicated, there are two kinetically important steps along the reaction coordinate controlling the reaction dynamics. These are the formation of $I_1$ ($k_{act}$) and $I_2$ ($k_{sft}$) in the mechanism shown in Figure 8. Our technique measures the rate limiting rate constant directly. Therefore, the rate constants extracted from the long exponential profiled in Figure 12, could be either $k_{act}$ or $k_{sft}$. To approximate the rate constant value which is not directly measured by this technique, and to quantify the induction times evident in the precursor decay profiles, software was developed to simulate the precursor decay waveform under instrumental conditions.

Figure 8 is a mechanism of consecutive steps to produce $Ni^+CO$ and ethane from the precursor $Ni^+(Ac)$. The solutions to the differential rate equations that govern precursor loss and fragment production have been solved for this type of system by Harcourt and Esson and were shown previously. These rate equations represent a model, that when programmed, result in software that produces three waveforms: precursor depletion (eq 3.5), the buildup and depletion of the first intermediate (eq 3.6), and fragment production (eq 3.7). The program generates a fourth waveform by integrating

fragment production under instrumental conditions, thus simulating observation. One of the rate constants is fixed by the value determined through regression analysis while the remaining two input parameters ($(Ni^+(Ac))_0$, $k_{act}$ or $k_{sft}$ ) are adjusted until the contour of the simulated waveform overlays the experimental waveform. However, there are no combinations of the input values that provide adequate simulation of the observed waveform. It appears that direct application of the rate eqs 3.5-3.7 is incapable of modeling the early portions of the decay.

The character of the of the depletion waveforms indicates that fragment ions are not immediately produced, as indicated by eq 3.7. Therefore, to improve the model, an induction period is implemented that delays fragment production as indicated by eq 3.9. It is assumed that this delay correlates with the time of maximum intermediate production; thus, fragments are not observed in sufficient quantity until the intermediate has reached maximum concentration. The program is modified to incorporate this induction time. Application of the improved model adequately simulates the experimental waveforms as shown in Figures 14 and 15. Again, one rate constant ($k_{act}$ or $k_{iso}$) is fixed by the value measured directly and the remaining two parameters (the initial concentration and the remaining rate constant) are adjusted until agreement between simulation and experiment is visually confirmed.

$$t_{ind} = \frac{\ln\left(\frac{k_{sft}}{k_{act}}\right)}{k_{sft} - k_{act}} \tag{3.9}$$

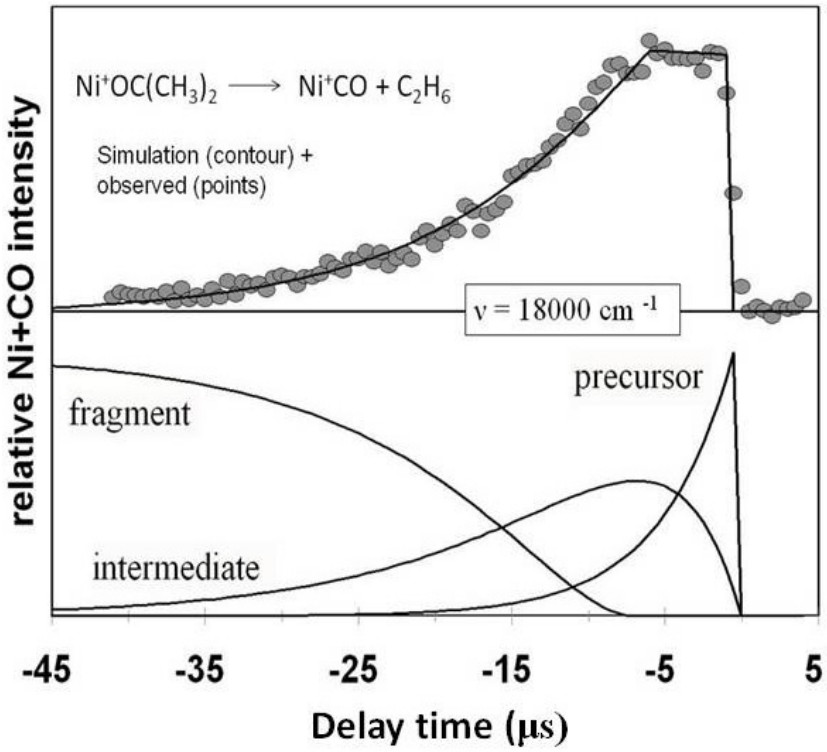


Figure 14. Top panel: The $Ni^+$($h_6$-Ac) fragment growth waveform shown with simulation The photon energy used to initiate the reaction is 18000 $cm^{-1}$. Bottom panel: The three waveforms showing precursor depletion and the gradual building and depletion of a long lived intermediate. Fragment ion buildup is also shown, which is delayed until the intermediate has reached the maximum concentration.

The top panel of Figures 14 and 15 shows the simulated (solid curve) superimposed upon the observed (points) in the $Ni^+$($h_6$-Ac) and $Ni^+$($d_6$-Ac) growth waveforms respectively. The photon energy used to initiate the reaction is 18000 $cm^{-1}$ for both systems. The lower panel displays the precursor and intermediate waveforms generated from eqs 3.5 and 3.6. The fragment production waveform is from eq 3.7; however, this waveform is delayed by the induction period which correlates with maximum intermediate concentration. The rate constants used to generate the simulated waveform in Figure 14 are $k_{act} = 20.0 \times 10^4\ s^{-1}$ and $k_{sft} = (9.68 \pm 0.03) \times 10^4\ s^{-1}$, where $k_{sft}$

was held constant at the value acquired through regression analysis. The rate constants (labeled as $k_{act}$ and $k_{sft}$), as well as the induction times, can be seen in Table 2.

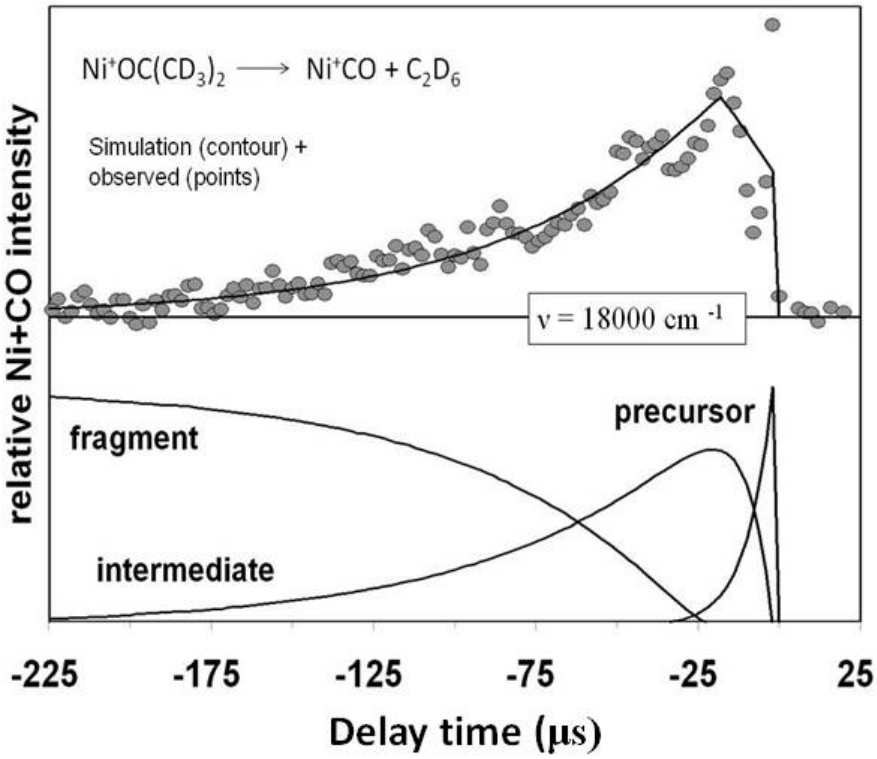


Figure 15. Same type of kinetic simulation shown in Figure 14 except for the unimolecular decomposition of $Ni^+$($d_6$-Ac) precursor ion.

The observed $Ni^+$($d_6$-Ac) waveform is shown in the top trace of Figure 15. The solid lines are simulated using the same modeling software. Again, fragment production (bottom trace) must be delayed until the intermediate has reached maximal concentration in order to adequately reproduce the early portions of the decay waveform. The induction period and relatively small rate constants are responsible for the apparent cusp in the simulated and observed precursor ion decay waveforms in the top panel of Figure 15. The rate constants used in the simulation, as well as the resulting induction periods, are shown in Table 2.

*Summary*

Kinetic measurements associated with the $Ni^+$ assisted decomposition of acetone have been presented. The rate limiting step in the low energy reaction to form neutral ethane gas and $Ni^+CO$ from the electrostatic bound $Ni^+(Ac)$ complex is the methyl group migration leading to C-C bond coupling. This step follows the activation of the C-C σ-bond. It was determined by measuring the unimolecular decomposition rate constants for both the $Ni^+(h_6\text{-Ac})$ and the deuterium labeled $Ni^+(d_6\text{-Ac})$ species under similar conditions and excitation energies. The results showed that both C-C bond activation and the methyl group migration are kinetically important. The rate constant associated with bond activation was determined through simulation. The kinetic isotope effect (KIE) was calculated for both processes yielding a KIE of nearly 2 for C-C bond activation and an averaged value of ~5.5 for the rate limiting step.

# CHAPTER FOUR

## $Co^+$-Assisted Decomposition of $h_6$-acetone and $d_6$-acetone: Acquisition of Reaction Rate Constants and Dynamics of the Dissociative Mechanism

This chapter reproduced in part with permission from:

- Villarroel, O. J.; Laboren, I. E.; Bellert, D. J. *J. Phys. Chem. A* **2011**, submitted for publication.

### *Introduction*

Essentially every useful chemical process initiates by breaking the bonds between certain atoms in a molecule. Indeed, in both biological and industrial processes where a certain product is required, significant effort is spent in selecting the appropriate bonds to break at minimal energy costs. This desire for selectivity at lowered activation energies is the driving force behind catalytic research.

The use of transition metals in catalyzing organic bond fragmentation reactions is well documented. Gas phase experiments, where careful control of the environment and energy content of the system is possible, provide an understanding of the energy lowering ability of transition metal active sites and the associated reaction mechanism. Ion cyclotron resonance mass spectrometry,[12-24] and ion beam studies using tandem mass spectrometry,[25-47] are such gas phase experiments. In these techniques, products are sampled following the reacting collision of a transition metal and organic species. Selective isotopic labeling of the organic reactant results in product distributions, suggesting mechanistic steps along the reaction coordinate.

More recently, measurements of product kinetic energy release distributions (KERDs) suggest the activation energy requirements in such $M^+$-organic reactions.[34-37]

Bowers *et. al.*[34] measured the KERD for the $CoCO^+$ and $Co^+(C_2D_6)$ product ions following the decomposition of metastable $Co^+(OC(CD_3)_2)$. The authors fit to the observed KERD suggested that the activation energy for this reaction is 43 kcal/mol (15000 $cm^{-1}$). It was further suggested that the oxidative addition to the C-C □-bond was the rate-limiting step in this reaction.

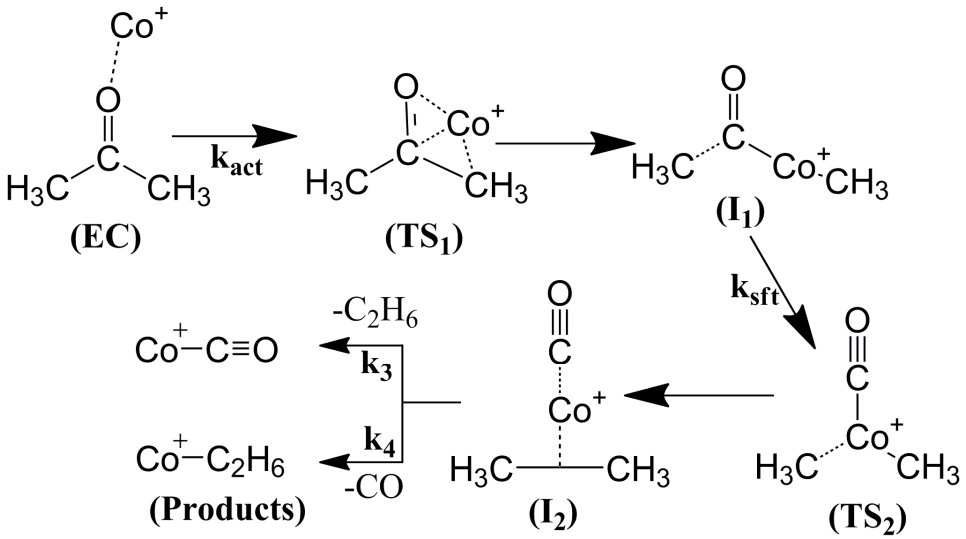


Figure 16. $Co^+$-assisted dissociative mechanism of acetone.

The results presented here represent the first direct measurements of the unimolecular decomposition kinetics for the $Co^+$-acetone ($Co^+(Ac)$) cluster ion. Our unique technique provides a direct determination of the rate-limiting rate constant at well resolved cluster internal energies. It is likely that the decomposition reactions follows the mechanism presented in Figure 16.[13, 19, 34] Upon receipt of energy in excess of the activation requirements, the encounter complex (EC) transitions to the first intermediate ($I_1$). The rate constant to form the transition state that separates the EC from $I_1$ is labeled $k_{act}$, indicating the activation of the C-C □-bond. The second transition state results as a methyl group transiently bonds to the cation. The rate constant controlling this process is

labeled $k_{sft}$. Formation of the second intermediate ($I_2$) follows as the two methyl groups bond couple, forming an electrostatic complex between an ethane molecule and the $Co^+CO$ ion. The final step breaks one of these electrostatic bonds forming the products without significant rearrangement of $I_2$.

*Experimental Section*

These experiments were performed in a custom time of flight mass spectrometer (TOFMS) which has been described previously.[65] The $Co^+(Ac)$ precursor cluster ions are generated in a jet-cooled expansion in a large vacuum chamber. The cold and isolated cluster ions absorb pulsed laser radiation. Fragment ions formed within the TOF are selectively detected following transmission through a voltage tuned, hemispherical sector.

Specifically, the supersonic source chamber is a 120 liter vacuum chamber (operational pressures ~ $3x10^{-6}$ torr). An external motor couples motion into the vacuum chamber and rotates a 5 mm solid cobalt rod (99.95 % purity) at a rate of 1.1 rpm. The rotational motion is defined by high precision bearing rings press fit into an open configuration stainless steel source block. A high pressure line is coupled into the vacuum chamber that connects to the source block through a Series 9 General Valve. The valve/rod assembly is centrally located in this main vacuum chamber. Momentarily opening the solenoid valve allows high pressure (~100 psi) helium gas, doped with acetone vapor, to supersonically expand into the vacuum chamber. As the expansion plume develops, 248 nm laser radiation from a pulsed KrF excimer is focused onto the rotating metal rod, ablating the metallic surface and seeding neutral and ionic cobalt atoms into the expansion. The substantial number of collisions between the doped carrier

gas and atomic $Co^+$ ensures the formation of $Co^+(Ac)_n$ clusters. Figure 17 presents a typical mass spectrum acquired during this study. The large pressure drop ($10^9$) between the static gas reservoir and the vacuum assures that the cluster ions are formed with minimal amounts of internal energy. Source conditions are optimized to form the coldest ionic clusters possible with stable concentrations. This is done by minimizing the distribution of precursor ion velocities in the beam and has been described previously.[64]

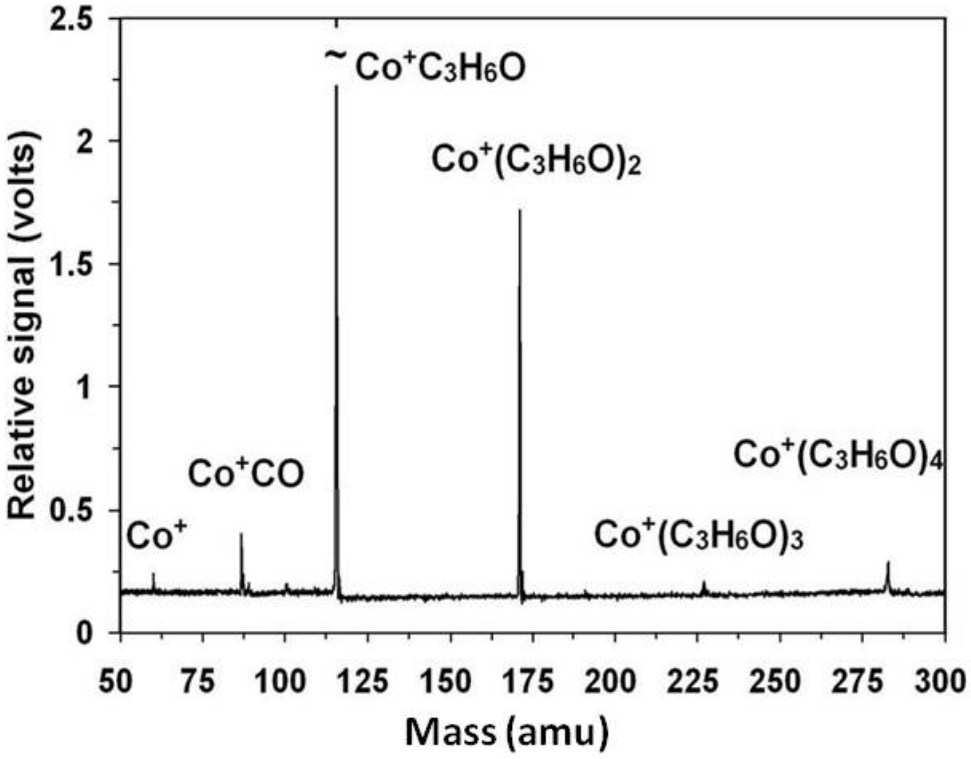


Figure 17. $Co^+(Ac)_n$ precursor ion time-of-flight mass spectrum.

The supersonic expansion is skimmed twice as the beam approaches a Wiley-McLaren[69] type orthogonal accelerator (OA). Pulsed laser radiation from a $Nd^{3+}$:YAG pumped dye laser counterpropagates to, but is co-linear with, the molecular beam. The pulsed laser is timed to intersect the cluster ions at various locations before the precursor ions enter into the TOF. Cluster ions absorb the radiation and unimolecular

decomposition into fragments ensues. Only those fragments formed after acceleration will be selectively detected following transmission through a voltage tuned hemispherical sector. This sector is located at the exit of the 1.8 meter length TOF. The cylindrical channel through the sector terminates in a Chevron microchannel plate detector. Sampling only those fragment ions that are formed during this 1.8 meter field free flight provides the signals acquired in this study.

Fragment production waveforms are generated by a computer controlled scan of the timing delays. The program monitors the intensity of selected fragments transmitted through the sector while the dye laser is temporally scanned relative to the OA voltage pulse. Thus, the fragment intensity is plotted versus the time delay between the triggering pulses to the OA and YAG laser.

*Results*

The results of the low-energy, $Co^+$ assisted decomposition of acetone and its deuterium labeled isotope are presented. These unimolecular decomposition reactions result in the formation of two charged fragments and corresponding neutrals as shown in rxns 8-11.

$$Co^+(OC(CH_3)_2 \longrightarrow Co^+CO + C_2H_6 \quad \textbf{(rxn 8)}$$

$$\longrightarrow Co^+(C_2H_6) + CO \quad \textbf{(rxn 9)}$$

$$Co^+(OC(CD_3)_2 \longrightarrow Co^+CO + C_2D_6 \quad \textbf{(rxn 10)}$$

$$\longrightarrow Co^+(C_2D_6) + CO \quad \textbf{(rxn 11)}$$

The secondary mass resolution of this instrument is sufficient to separate the charged fragments that result from rxns 10 and 11 (Panel A, Figure 6). Sampling these products yielded common rate-limiting rate constants, suggesting that either the oxidative addition ($k_{act}$) or the rearrangement ($k_{sft}$) is the rate-limiting step in the mechanism of Figure 16.

The fragment masses of rxns 8 and 9 are unresolved through our sector. Thus, all fragment yields for the $Co^+$ assisted decomposition of $h_6$-acetone result from the combined sampling of these two product channels. This has no effect on the measured kinetics as these reactions are not rate-limited by the dissociation of the electrostatic bond in $I_2$ of Figure 16. Thus, the distinction between sampling $Co^+CO$ or $Co^+(C_2H_6)$ from the assisted decomposition of $h_6$-acetone is not further considered.

Two types of laser, photodissociation experiments are conducted here: direct dissociation and the $Co^+$ assisted rearrangement decay. Direct dissociation follows the absorption of one or several high energy photons, causing electronic transition into an unbound state. No kinetic barriers separate the products from reactant and these results in fast, bond-cleavage dissociation. The $Co^+$ assisted rearrangement decay occurs as the ionic cluster absorbs a quantum of photon energy to initiate the reaction. Organic bonds are activated and atoms rearrange within the excited cluster, forming the decomposition products. Assisted decay requires mounting kinetic barriers during molecular rearrangement. Thus this process is relatively slow in comparison to direct dissociation.

Experimentally, fragments that result from direct dissociation are primarily sampled when laser radiation overlaps the counter-propagating ion beam along the TOF axis. Whereas rearrangement decay is sampled when pulsed laser radiation overlaps the counter-propagating molecular beam along the expansion axis. These different experiments result in different fragment yields as seen in the panels of Figure 6. Figure 6 identifies the fragment ions that transmit through the kinetic energy filter as the potential difference across the halves of the sector is voltage tuned. Panel B shows fragment ions that primarily result from the direct dissociation of $Co^+(OC(CD_3)_2)$ as intense UV laser radiation (28200 $cm^{-1}$, 20 mJ/pulse) intersects the precursor ions 500 ns before entrance

into the sector. This scan is dominated by loss of $Co^+$ but also contains contributions from $Co^+CD_3$ as well as $Co^+CO$. Similar studies at lower energies (18800 $cm^{-1}$, 30 mJ/pulse) result in a slightly different fragment distribution; $Co^+CD_3$ is absent while $Co^+(C_2D_6)$ is present at low intensities.

These results suggest that there are two $Co^+(OC(CD_3)_2)$ geometries present in the beam at significant concentrations. One where the $Co^+$ atomic ion is attached to the acetone via an ion-dipolar bond (EC, Figure 16) and one where the $Co^+$ cation is attached to both a CO and $C_2D_6$ molecule in an electrostatically bound cluster ($I_2$, Figure 16). Both of these complexes can be formed in a laser-driven, jet-cooled expansion. Thus, the $Co^+$ and $Co^+CO$ ions in panel B of Figure 6 are the likely binary cleavage products resulting from direct dissociation of such electrostatic complexes. The photon energy (28200 $cm^{-1}$) is well in excess of these bond dissociation requirements (Table 3).

Table 3. Bond Dissociation Energies (BDE) of some Co+ complexes.

| Ligand | BDE ($cm^{-1}$) |
|---|---|
| $C_2H_6$ | 9800±560[a], 8400±400[b], 9230[c] |
| CO | 13675±1000[d], 14500±560[e], 13000[f], 11900±1000[g], 14000[h] |
| $CH_3$ | 21300±1400[i], 16928±315[j], 17319[k], 18600±700[l] |
| $(CH_3)_2CO$ | 18200±1000[d], 17800[h] |
| $CH_3CHO$ | 14935[m], 16400[h] |

[a]Ref 75. [b]Ref 76. [c]Ref 77. [d]Ref 34. [e]Ref 78. [f]Ref 79. [g]Ref 31. [h]Ref. 13. [i]Ref. 27. [j]Ref. 26. [k]Ref. 80. [l]Ref. 81. [m]Ref. 53

The presence of the $Co^+CD_3$ peak is somewhat unexpected (panel B, Figure 6); however, products resulting from intense UV photolysis are not always easy to predict. As the photon energy is reduced to visible radiation, the intensity of the $Co^+CD_3$ peak is diminished to baseline and a $Co^+(C_2D_6)$ peak appears. The resulting product yields in these lower energy photodissociation experiments support the conclusion that both the EC and $I_2$ are the complexes formed with significant concentration in the jet-cooled expansion.

Panel A of Figure 6 presents the fragment yield resulting from the photon initiated, $Co^+$ assisted, rearrangement decay of acetone. Here, 15900 $cm^{-1}$ of pulsed laser radiation (laser fluence ~25 mJ/pulse) is directed toward the clusters along the expansion axis. The laser radiation intersects the clusters three microseconds before pulsing the grid to a high positive potential. Any precursor ion that absorbs the radiation and dissociates before exiting the OA field produces fragment ions that are unable to transmit the sector. Thus, conducting the experiment in this fashion yields detectable fragments that must be formed from the relative slow decay of a precursor ion. The EC is the only cluster ion in the expansion where kinetic barriers separate products from the reactant. Thus, the EC is the title $Co^+(Ac)$ isomer that undergoes unimolecular decomposition yielding the kinetic results presented here.

*Identity of the precursor ion through theoretical calculation.* A search for the likely isomeric geometries of the precursor ion was conducted at the B3LYP level of density functional theory (DFT).[82] The minimized energy for the EC structure was determined using various basis sets (Table 4). These values appear to converge at ~16910 $cm^{-1}$. Therefore, all calculations were continued at the 6-311+G(2df, 2pd) basis

set level as this seems to present a logical compromise between basis set size, accuracy, and computation time. Calculations of the various spin states of the EC proved that the triplet state is the lowest in energy. This is consistent with the atomic energy level structure of $Co^+$; the $[^3F(3d^8)]$ (Table 1) is the ground state configuration.

Figure 18 shows the various minimized isomeric structures resulting from these calculations. The parenthetical values indicate the calculated energy associated with each structure and are relative to the encounter complex. Corrective computations to this energy were not sought as we are only concerned with the relative energies of each structure. Three local minima are identified and are labeled in accord with Figure 16.

Table 4. The triplet ground state energies ($cm^{-1}$) for the $Co^+$(Ac) encounter complex minimized at the B3LYP level of DFT using different basis sets.

| Basis Set | Energy ($cm^{-1}$) |
|---|---|
| 6-311+G(d,p) | 16545 |
| 6-311++G(d,p) | 16722 |
| 6-311+(2df, 2pd) | 16910 |
| 6-311++(2df, 2pd) | 16911 |

The two lowest energy $Co^+$(Ac) isomers are the encounter complex (EC) and the electrostatic intermediate ($I_2$). These are likely the isomers with the largest concentrations in the supersonically cooled beam. When energy in excess of each cluster bond is delivered to these isomers, the electrostatic bond is broken and fragments are formed without significant rearrangement. Such barrierless dissociations are likely too fast to be measured by the methods employed here. Rather, this technique is limited to measuring relatively slow events that evolve over the microsecond time-scale. As such,

the EC is the only isomer in the beam with an appreciable concentration that can undergo slow rearrangement decomposition into the fragments observed in panel A of Figure 6.

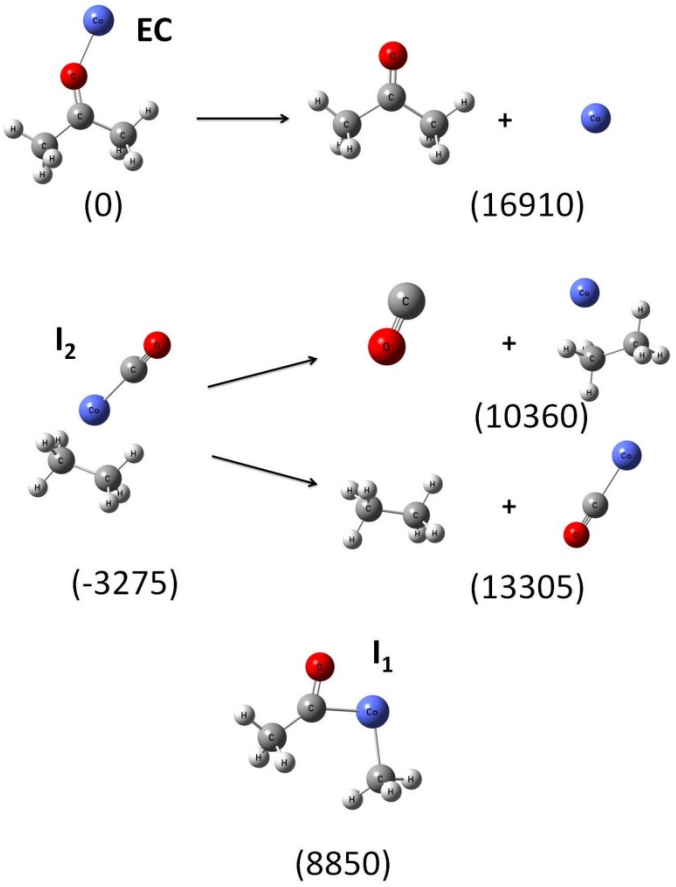


Figure 18. Energy minimized structures resulting from calculations performed at the B3LYP/6-311+G(2df ,2pd) level of theory. The parenthetical terms are wavenumber energies with respect to the encounter complex $Co^+$(Ac) isomer.

*Activation through photon absorption.* In this study, the activation energy is supplied to the cold cluster through photon absorption. A photon of laser radiation in the range of 12300 - 16100 $cm^{-1}$ is absorbed, electronically exciting the cluster. The lowest energy electronic excitation in acetone is the $\pi^* \leftarrow$ n transition at ~36000 $cm^{-1}$; this is too high in energy to be responsible for photon absorption here. Therefore, the $Co^+$ cation is the chromophore in this cluster. The atomic ground state term is $[3d^8(^3F)]$ (Table 1).

Spin and/or parity forbidden electronic excitation results in a metastable state. The cluster cannot release energy through direct dissociation into $Co^+$ + acetone as the absorbed energy is below the cluster bond energy. Additionally, selection rules prevent relaxation through photon emission. Rather, the excited state likely intersystem crosses to the ground potential surface, depositing the energy of the electronic transition (or the photon energy) into the high vibrational levels of the ground state. Energy deposition into these highly excited vibrational states provides the activation energy for the observed assisted dissociation of the cluster ion.

The precursor ions are formed as clusters, cooled through supersonic expansion. It is assumed that the absorbed photon energy is much larger that the thermal energy of the jet-cooled cluster such that the latter forms a negligible fraction of the internal energy of the photoexcited complex. Thus, the photon energy approximates the total energy available for chemical reaction. If this is in excess of the activation requirements, the precursor ion dissociates into fragments. The excited cluster ions experience first order decay with the precursor concentration developing in time according to eq 3.1.

*The $Co^+$ assisted decomposition kinetics of acetone.* Eq 3.1 describes the unimolecular decay of the photoexcited $Co^+$(Ac) precursor ion. The $Co^+$CO fragment ion is selectively sampled as the timing delay to fire the excitation laser is scanned relative to the OA charge pulse. The triggering pulse to bring the OA to full potential is defined as zero microseconds. The trigger pulse to fire the excitation laser precedes charging the OA and these time values are therefore recorded as negative delays. Thus, the intensity of the $Co^+$CO fragment ion is measured as the timing difference between pulsing these two devices is increased. The average of 100 experimental cycles is plotted as a point at

each delay setting. The two lower panels of Figure 19 show that the combination of these measurements result in a waveform consistent with the exponential behavior predicted by eq 3.1.

In Figure 19, zero microseconds represents the coincident firing of both the OA and excitation laser. As the difference in timing delay increases, the cold cluster ions absorb the laser radiation at greater distances from the OA. Fragment ions are formed as the precursor concentration decreases in time according to eq 3.1. Only the fraction of fragments that result from dissociation during the time following orthogonal extraction and entry into the sector will be sampled. Thus, the detected fragment ion intensities typically decrease as the timing difference to pulse the excitation laser increases.

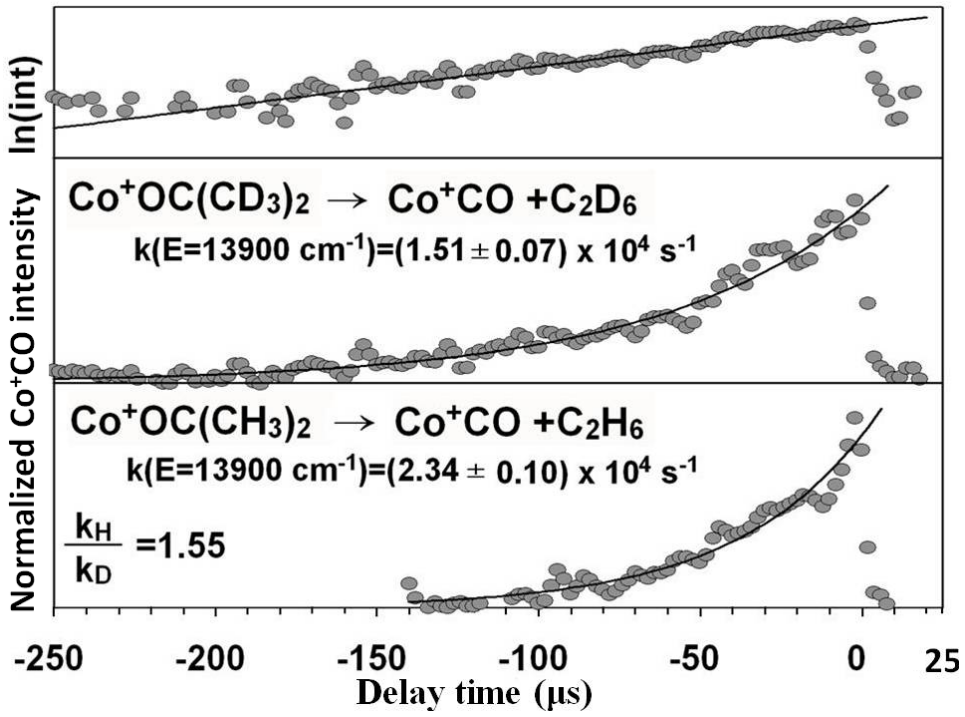


Figure 19. Bottom two panels: waveforms resulting from $Co^+$ assisted dissociative reactions of the two isotopic variants studied. Top panel: the waveform made linear by plotting the natural logarithm of the signal intensity vs. delay time.

The lowest panel of Figure 19 shows the waveform associated with the $Co^+$ assisted decomposition of $h_6$-acetone while the center panel shows the same for the assisted decomposition of $d_6$-acetone. Here, the production of $Co^+CO$ is monitored as the isotopic variants of the cluster absorb a photon with energy = 13900 $cm^{-1}$. It is obvious that each waveform expresses the exponential character of eq 3.1, but with different decay constants. The top panel of Figure 19 plots the natural logarithm of the fragment intensity versus time for the heavier isotope. A linear analysis of the measurements from 0 to -175 microseconds result in a slope value (k) and intercept ($A_0$) in accord with eq 3.1. These regression constants are used to generate the solid line and curve through the experimental points in the top two panels of Figure 19. The rate constant is reported in the figure as k(E=13900 $cm^{-1}$) = (1.51 ± 0.07) x $10^4$ $s^{-1}$. The error is extracted from the linear regression analysis and is equal to the first standard deviation in the slope. The rate constant is recorded at the photon energy absorbed by the cluster as this approximates the internal energy of the precursor ion.

Each waveform measurement is analyzed in similar fashion. The rate constants extracted from the linear fits represent the rate-limiting rate constant in the unimolecular dissociative mechanism. Rate constants for the assisted decomposition reaction are determined for both the $h_6$ and $d_6$ isotopic variants of acetone. The ratio of these rate constants, or the kinetic isotope effect, has a weighted average value of $k_h/k_d$ = 1.54 ± 0.05. These values are provided in Table 5.

The sequential mechanism presented in Figure 16 identifies two possible transition states: the step leading to oxidative addition with rate constant $k_{act}$, and the step leading to reductive elimination ($k_{sft}$). To identify which step is likely rate-limiting, comparisons to the similar $Ni^+$ assisted decomposition of acetone are made.[65, 66] Figure

20 plots the fragment ion intensity sampled during the decomposition of $h_6$-acetone assisted by $Ni^+$ (top panel) and $Co^+$ (lower panel) at similar excitation laser energies (~16250 $cm^{-1}$). Although the dissociative mechanism is likely the same for these two systems,[19, 34] the dissimilar waveforms of Figure 20 indicate significant differences in the unimolecular decay dynamics.

Table 5. Rate constants (x $10^4$ $s^{-1}$) measured for the transition metal ion assisted, unimolecular decomposition of acetone and deuterium labeled acetone.

| Internal Energy ($cm^{-1}$) | $Ni^+(h_6$-Ac)[a] | | $Ni^+(d_6$-Ac)[a] | | $k_H/k_D$ | | $Co^+(h_6$-Ac)[b] | $Co^+(d_6$-Ac)[b] | $k_H/k_D$ |
|---|---|---|---|---|---|---|---|---|---|
| | $k_{act}$ | $k_{sft}$ | $k_{act}$ | $k_{sft}$ | act | sft | $k_{act}$ | $k_{act}$ | act |
| 18800 | 22 | 11.7±0.8 | | | | | | | |
| 18000 | 20 | 9.68±0.3 | 12.5 | 1.60±0.08 | 1.6 | 6.1 | | | |
| 17700 | 20 | 9.27±0.3 | | | | | | | |
| 16800 | | 6.33±0.3 | | | | | | | |
| 16400 | 13 | 6.10±0.2 | 6.7 | 1.17±0.06 | 1.9 | 5.2 | | | |
| 16100 | | 5.80±0.3 | | | | | 9.70±0.6 | 6.41±0.3 | 1.51 |
| 15900 | | | | | | | 8.92±0.7 | 5.8±0.5 | 1.54 |
| 15600 | | 5.60±0.3 | | | | | 8.7±0.6 | 5.76±0.3 | 1.51 |
| 14300 | | | | | | | 2.58±0.3 | 1.62±0.2 | 1.59 |
| 13900 | | | | | | | 2.34±0.1 | 1.51±0.07 | 1.55 |
| 13700 | | | | | | | 2.13±0.1 | 1.36±0.08 | 1.57 |
| 12900 | | | | | | | 2.00±0.5 | | |

[a] Ref. 65 and 66. [b]This study.

A two transition state model was adopted to describe the waveform measured for the $Ni^+$ assisted decay of acetone.[65, 66] The rate constant associated with each kinetic barrier was similar in magnitude and this resulted in an induction period that delayed fragment formation. This induction time causes a featureless plateau at early delay values. The rate-limiting step, however, resulted in decay over relatively long periods of time and is responsible for the long exponential portion of the waveform in the top panel

of Figure 20. This rate constant, and associated error, was extracted from this exponential decay. As described previously, the natural logarithm of the fragment intensity was fit to a straight line and the measurements from -15 to -55 microseconds was regressed to yield the rate-limiting rate constant, k(E = 16400 $cm^{-1}$) = (6.1 ± 0.2) x $10^4$ $s^{-1}$.

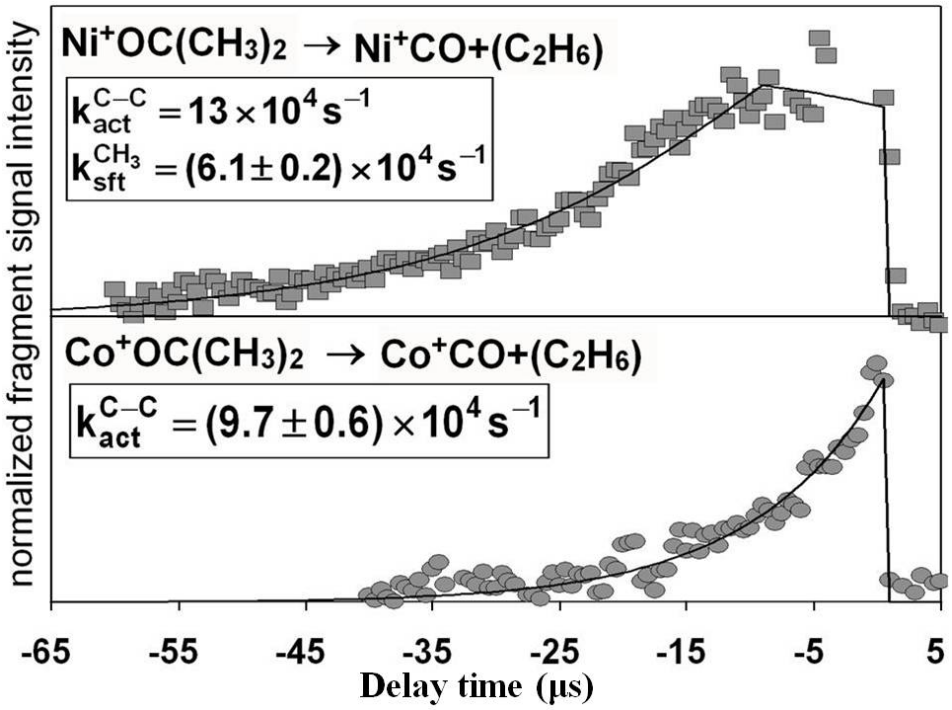


Figure 20. Comparisons between the $Ni^+$ (top panel) and $Co^+$ (bottom panel) assisted decomposition of acetone performed at similar excitation energies: 16400 $cm^{-1}$ and 16100 $cm^{-1}$ respectively. Extracted rate constants are indicated in each panel.

The remaining rate constant in this assisted decomposition reaction was extracted through simulation of the observed waveform.[66] Time dependent concentration terms for the precursor, intermediate, and products were determined by solving the kinetic equations for a sequential two-step mechanism. An induction period was incorporated into this model by delaying product formation until the intermediate concentration reached its maximum value. This model was programmed into software that calculated a

waveform based on how fragment ions are sampled by our technique. The program requires three input parameters: two rate constants and the initial precursor concentration. One of the rate constants is held constant at the experimentally determined value while the remaining two parameters are adjusted until the simulated contour superimposes upon the measured waveform. This simulation is shown in the top panel of Figure 20 as the solid curve through the measured points. The rate constant that provided the best fit is recorded in the figure as 13 x $10^4$ $s^{-1}$. These measurements were taken over a range of laser energies and are provided in Table 5.

To determine whether the step leading to oxidative addition ($k_{act}$) or that leading to reductive elimination ($k_{sft}$) was rate-limiting, rate constants for the $Ni^+$ assisted decomposition of deuterium labeled acetone were measured. These experiments and analyses were carried out as described earlier.[66] These results provided two rate constants and thus, two determinations of the kinetic isotope effect. The rate-limiting $k_h/k_d$ averaged ratio was 5.5 while the other was ~1.8 (Table 5). The isotopically labeled species in these systems are the methyl groups. The mechanistic step that requires the largest amplitude motion for this labeled species is the cation mediated, $CH_3$-shift. Since the rate-limiting step presents a kinetic isotope effect with a larger ratio magnitude, the rate-limiting step must involve this larger amplitude motion associated with the labeled species. This rationale assigns the methyl shift ($k_{sft}$) as the rate-limiting step in the $Ni^+$ assisted reactive dissociation of acetone. This assignment is in agreement with recent theoretical calculations of this reaction coordinate.[49]

The comparative study of Figure 20 indicates that the dynamics of these two similar systems are different. A two transition state model describes the formation of $Ni^+CO$ product whereas formation of $Co^+CO$ is limited by a single kinetic barrier. The

kinetic isotope effect measured for the $Co^+$ assisted decomposition of acetone has an averaged value of 1.54 ± 0.05. This value is similar to the kinetic isotope effect determined for the $Ni^+$ activation of the C-C □-bond of acetone (~1.8, Table 5). Additionally, the magnitudes of the C-C activation rate constants determined for the comparable $Ni^+$ system are similar to the rate constants extracted directly from the waveforms acquired in this study (Figure 19, Table 5). These similarities, both in the ratio magnitude of the kinetic isotope effect as well as in the value of these rate constants, suggest that the reactive decomposition of $Co^+$(Ac) is rate-limited by C-C bond activation and not by the cation mediated, $CH_3$-shift. This assignment is consistent with earlier KERDs measurements on this system.[34]

*Discussion*

Figure 20 compares the rearrangement dissociation of acetone by the $Co^+$ and $Ni^+$ cations. The dynamics associated with each system is unique despite the likelihood of a common dissociative mechanism. Comparison of the kinetic isotope effect measured in the assisted dissociation of acetone suggests that C-C □-bond activation rate-limits when the $Co^+$ cation mediates the reaction, while the $CH_3$-shift rate limits the $Ni^+$ assisted decomposition reaction.[66] The dynamical differences between these similar systems must be attributable to the different electronic structures of each cation.

The low-lying electronic structures of $Ni^+$ and $Co^+$ are compared in Figure 21. The ground electronic state of $Ni^+$ is $[3d^9(^2D)]$ while $Co^+$ is $[3d^8(^3F)]$ (Table 1). These metals likely remain in these atomic configurations during initial complexation with acetone in the source. Thus, the spin and angular momentum of the ground state of the encounter complex (Figure 16) is the same as that for each atomic ion. During formation

of the first intermediate ($I_1$ -Figure 16) the transition metal forms two covalent bonds; one with the carbonyl carbon and the other with the methyl carbon. The DFT calculated C-M-C bond angle for these inserted species are 100° ($Co^+$) and 113° ($Ni^+$).[49] These are larger than the expected bond angles when only pure d-orbitals are involved in bonding.[83] Thus, we assume that the bonding in this intermediate is governed by either sd hybridization or some other mechanism that widens these angles. Indeed, the DFT calculated reaction coordinate for the $Ni^+$ assisted dissociative reaction suggests sd hybridization at the $Ni^+$ atom to form this intermediate.[49]

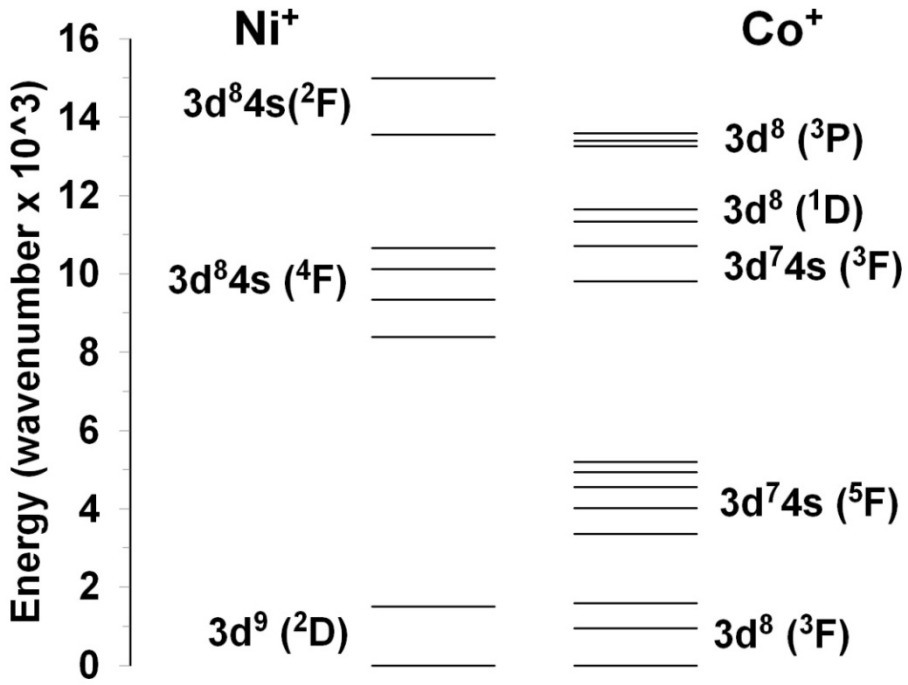


Figure 21. $Ni^+$ and $Co^+$ atomic energy levels and terms.

Although the coordinate for the $Co^+$ assisted dissociation of acetone has yet to be calculated, the bonding associated with species similar to $I_1$ (Figure 16) has been determined at high levels of theory.[84] The $Co^+(CH_3)_2$ cation has been theoretically studied and the bonding between the metal center and the carbon atoms was shown to be

sd hybrids. However, a subsequent study,[85] calculated an inequivalence between the two $Co^+$-C bonds and suggested that the bonding to the methyl groups primarily occurs through a Co 4s-like orbital and the other through a Co 3d-like orbital. This latter study suggested that inefficient hybridization of the 4s and 3d orbital (due to dissimilar sizes) necessitates this inequivalent bonding and this occurs primarily through promotion to the [ $3d^7 4s(^5F)$] excited state of $Co^+$. Both of these bonding schemes leave four non-bonding orbitals of metal character. It is interesting to note that the electrons from the metal may occupy these non-bonding orbitals in such a way as to preserve the total spin and angular momentum associated with the ground state encounter complex.

As the first intermediate progresses to the second, the reaction must pass through the second transition state ($TS_2$ -Figure 16). It is the formation of this transition state that rate-limits product formation from the $Ni^+$ assisted decomposition of acetone. This transition state is tri-coordinate and forms transient bonds with the carbons of two methyl groups and the carbonyl. The logical progression is to assume that the transition metal ion adopts either an $sd^2$ hybridization or further electronic promotion to support the additional bond. However, this energy cost outweighs any gains in bonding.[84] Thus, the metal ions likely return to an atomic configuration that can support these bonding interactions. In order to keep the spin and orbital angular momentum constant, the metal likely assumes a $d^{n-1}s$ configuration of higher multiplicity. Here the metal bonding to the methyl groups will either occur through d-like or s-like orbitals. The CO bond in $TS_2$ shortens, approaching the gas phase carbon monoxide bond length. This suggests that the metal bonding to CO becomes electrostatic (as opposed to electron sharing) and the metal ion presents a d□ or d□ orbital along the M-CO bonding axis to minimize electronic repulsion. The increased repulsions between the CO and the $CH_3$ groups in this tri-

coordinate transition state likely decreases the $H_3C$-M-$CH_3$ bond angle facilitating C-C bond coupling to form the second intermediate.

We believe that it is the energetic promotions associated with this second step (formation of $TS_2$) that lead to the dynamic differences observed during the $M^+$ decompositions of acetone. The dissociation of acetone induced by the $Co^+$ ion is rate limited by initial C-C □-bond activation (formation of $TS_1$) while that for the $Ni^+$ is rate-limited by the $CH_3$-shift (formation of $TS_2$). From the mechanism and the description of the bonding, when $Co^+$ forms the first intermediate as the EC progresses through $TS_1$, the cation likely promotes to the [ $3d^7 4s(^5F)$] excited state to support two $Co^+$-C □-bonds. As the $I_1$ transitions to the second intermediate though $TS_2$, the $Co^+$ cation maintains this electronic configuration and has already paid the energy promotion costs in the first step. Contrast this situation to that of $Ni^+$. Theory predicts that the formation of $I_1$ involves sd hybridization.[83] When $I_1$ transitions to the tri-coordinate $I_2$ complex, the $Ni^+$ cation likely adopts an atomic configuration of higher multiplicity to preserve angular momentum and spin along the reaction coordinate. This involves promotion to the $^4F$, $Ni^+$ configuration. The lowest spin-orbit component of $Ni^+$ [ $3d^8 4s(^4F)$] is 8394 $cm^{-1}$ above the ground state whereas the lowest spin orbit component of $Co^+$ [ $3d^7 4s(^5F)$] is 3351 $cm^{-1}$ above the ground state configuration (Table 1 and Figure 21). Thus, we believe that it is the differences in bonding during the formation of $TS_2$, coupled to the energetic costs to promote to the $d^{n-1}s$ configurations of higher multiplicity, that account for the dynamic differences observed during these decomposition reactions.

*The energy to activate the C-C □-bond in acetone.* The results presented here indicate that the $Co^+$ cation assists in the dissociation of acetone by lowering the reaction

activation energy requirements. This fairly new experimental technique creates the reactants as a jet-cooled cluster, trapped in the deep potential energy well of the encounter complex. Calculations and experiments place this well depth at ~18000 $cm^{-1}$ (Table 3) and this approximate bond energy is the upper limit to the reaction activation energy. Energy supplied in excess to this limit should result in the simple cleavage of the $Co^+(Ac)$ cluster bond. The results of this study lower this upper limit to 12300 $cm^{-1}$, the lowest laser frequency where the cation assisted decay of acetone was monitored. This rate constant is $k(E = 12300\ cm^{-1}) = (2.0 \pm 0.5) \times 10^4\ s^{-1}$. The signal to noise ratio is lower here due to the relatively weak laser photon fluence of our dye laser at this frequency.

Previously, the activation energy for the $Co^+$ + acetone reaction has been estimated from fragment kinetic energy release distributions (KERDs).[34] The KERD was acquired for both $Co^+CO$ and $Co^+(C_2D_6)$ fragments resulting from the dissociation of metastable $Co^+(OC(CD_3)_2)$. The authors modeled the distribution using phase space theory and assumed the same oxidation/reductive elimination mechanism in Figure 16. These results, in combination with an estimated $Co^+(Ac)$ cluster bond strength, suggested a value of ~15000 $cm^{-1}$ (43 kcal/mol) for the reaction activation energy. The authors associated this energy with the $Co^+$ activation of the C-C □-bond and suggested that this was the rate-limiting step along the dissociative reaction coordinate.

Additionally, the energy associated with C-C □-bond activation via the $Co^+$ cation has been determined to the similar $Co^+$-acetaldehyde system.[49] Here, the authors calculate a potential energy surface where the dissociative reaction initiates with C-C □-bond activation and ultimately forms the products $Co^+CO + CH_4$. The C-C bond

activation energy calculated for this similar system is 13600 $cm^{-1}$ (38.9 kcal/mol). These determinations are provided in Table 6.

Table 6. The $Co^+$ C-C σ-bond activation energy ($cm^{-1}$) in acetone and acetaldehyde.

| System | $Co^+(OC(CH_3)_2)$ | $Co^+(OCH(CH_3))$ |
|---|---|---|
| Activation Energy ($cm^{-1}$) | 12300[a]; 15000[b] | 13600[c] |

[a] upper limit (this study). [b]Ref. 34. [c]Ref. 53

*Summary*

Kinetic measurements associated with the $Co^+$ assisted dissociation of acetone have been presented. These studies directly measure the rate-limiting rate constants as a function of internal energy and are the first of their kind for this system. A common mechanism has been previously proposed for such metal ion induced, acetone decomposition reactions. The size of these systems allows predictions of the reaction coordinate and the proposed mechanism is somewhat obvious. Despite the simplicity of these systems, the direct kinetic study of the reaction yielded interesting differences in the dissociation dynamics of two very similar systems: $Co^+$ and $Ni^+$ assisted decomposition of acetone. The different unimolecular decay dynamics are not likely attributable to different reaction coordinates followed to dissociation, but rather, due to the different electronic structure of each atomic ion. The key mechanistic step in the reaction potential energy surface is the formation of the tri-coordinate metal cation. The different energy costs to promote to a $d^{n-1}s$ configuration of higher multiplicity is postulated as the reason for the different dissociation dynamics between these similar systems.

Measurements of the kinetic isotope effect and comparative studies are used to assign C-C □-bond activation as the rate-limiting step in this acetone decomposition reaction. For $Co^+$ to activate acetone, the complex must possess sufficient energy for the cation to move away from the dipolar field of the acetone molecule and approach the C-C □-bond. The initial energy costs associated with this motion and activation of the single bond is compensated for by formation of two $Co^+$-C bonds. It is the balancing between these electrostatic and chemical forces that forms an energy saddle point along the reaction coordinate. The upper limit to this activation energy is the cluster bond strength as no reaction would occur if this saddle point energy was above the $Co^+$/acetone separated limit. The measurements conducted here lower this upper limit to 12300 $cm^{-1}$.

*Acknowledgments*

We gratefully acknowledge research support from the ACS Petroleum Research Fund (44393-G6). Additionally, we thank John R. Gillis, III for his Gaussian calculations and incite which forwarded this manuscript. Finally, the reviewers careful reading of this manuscript and insightful comments are appreciated.

CHAPTER FIVE

# Preliminary Results for the $Ni^+$-assisted Decomposition of Cyclopentanone in the Gas Phase: A Ring-Opening Reaction

## *Introduction*

The photochemistry of isolated gaseous cyclopentanone has been investigated since 1935.[86-93] Upon irradiation with ultraviolet light, gaseous cyclopentanone decomposes to give ethylene, cyclobutane, and carbon monoxide; it also rearranges to form 4-pentenal. This is presented in rxns 12-14. However, preliminary studies in our lab have revealed that the interaction of cyclopentanone with the $Ni^+$ cation lowers these energy requirements into the visible frequency range.

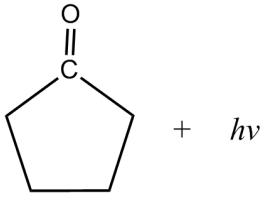

+ *hv*

$\longrightarrow$ $2C_2H_4$ + CO (rxn 12)

+ CO (rxn 13)

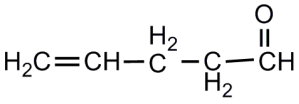

(rxn 14)

The study of the decomposition of cyclic ketones assisted by transition metals in the gas phase is not novel. In fact, these decomposition reactions have been studied over the last two decades.[12, 13, 18-20, 26, 29, 47] The previous studies have focused on the reactivity and stability of the intermediates, as well as the elucidation of fragmentation patterns. The relative abundance of daughters was also determined. However, no study has been conducted in the gas phase where kinetic parameters of these chemical reactions are measured.

The decomposition of cyclic ketones from collisions with transition metal ions has been studied extensively by Freiser,[18-20, 29] Beauchamp,[12, 13, 47] and Armentrout[26] using ion cyclotron resonance (ICR) mass spectrometry, and tandem mass spectrometry. These experimental chemists have used $Fe^+$, $Co^+$, $Ni^+$ and $Cu^+$ atomic ions in their studies. The proposed mechanism for the decomposition of cyclic ketones is similar to those proposed for the decomposition of cycloalkanes and various alkanes larger than butane. A common step in these mechanisms involves the formation of metallacycles as intermediates in the reaction. The formation and fragmentation of metallacycles is an important class of organotransition-metal reactions since these processes are involved in a number of significant catalytic transformations. Olefin metathesis, hydrocarbon cracking, isomerization, epoxidation, deepoxidation, and olefin dimerization are some of the processes believed to proceed through the intermediacy of metallacycles.

Although the reaction of different cyclic ketones with the before mentioned cations have been extensively studied, this chapter focuses on the reaction between $Ni^+$ and cyclopentanone. Beauchamp et al.[12] reported three different products for the CID reaction between $Ni^+$ and cyclopentanone in the gas phase. Decarbonylation is the primary dissociative process (rxn 15). In this reaction the $Ni^+C_4H_8$ ion is formed which may have a metallacycle structure; however this was not concluded in that work. A second process involves dehydrogenation following decarbonylation (rxn 16). The final reaction channel eliminates $C_4H_8$ (rxn 17) with the formation of the charged fragment $Ni^+CO$. Reactions 15-17 show the product distribution for the reaction of $Ni^+$ with cyclopentanone.

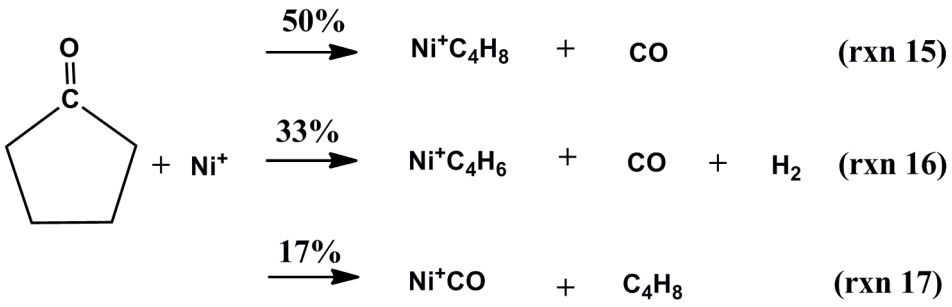


However, utilizing ICR spectroscopy and Fourier transformer mass spectrometry, Freiser et al.[20] proposed a different dissociative mechanism. They suggest that metallacycles are intermediates in the decomposition of cyclopentanone in collision with the nickel cation. The reaction between nickel cation and cyclopentanone initiates by forming a $Ni^+$-cyclopentanone complex (rxns 18 and 19). This is followed by insertion into an α-C-C bond, thus forming a six member ring. Carbonyl abstraction then occurs with competitive elimination of CO (39%), $C_2H_4$ (13%) and $H_2$ (48%).

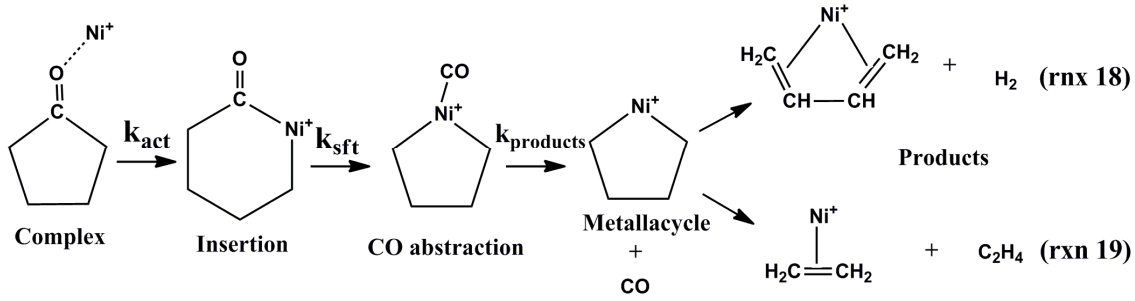


Rxns 18 and 19 suggest the formation of a metallacycle as a common reaction intermediate ($Ni^+C_4H_8$). Metallacyclopentanes have been previously synthesized in the gas phase by decarbonylation of cyclopentanone by $Fe^+$, $Co^+$ and $Ni^+$. In this specific experiment reported by Freiser, the metallacyclopentane intermediate decomposes upon collisional activation both by dehydrogenation and by symmetric ring cleavage ($C_2H_4$ elimination) as is shown in rxns 18 and 19 respectively. The dehydrogenation mechanism was probed using cyclopentanone α,α,α',α'-$d_4$. Dehydrogenation of

metallacyclopentanes may simply involve two sequential hydride shifts (rxn 21) or a 1,3-hydrogen atom shift may occur generating a metal ion complex, which readily dehydrogenates (rxn 22).

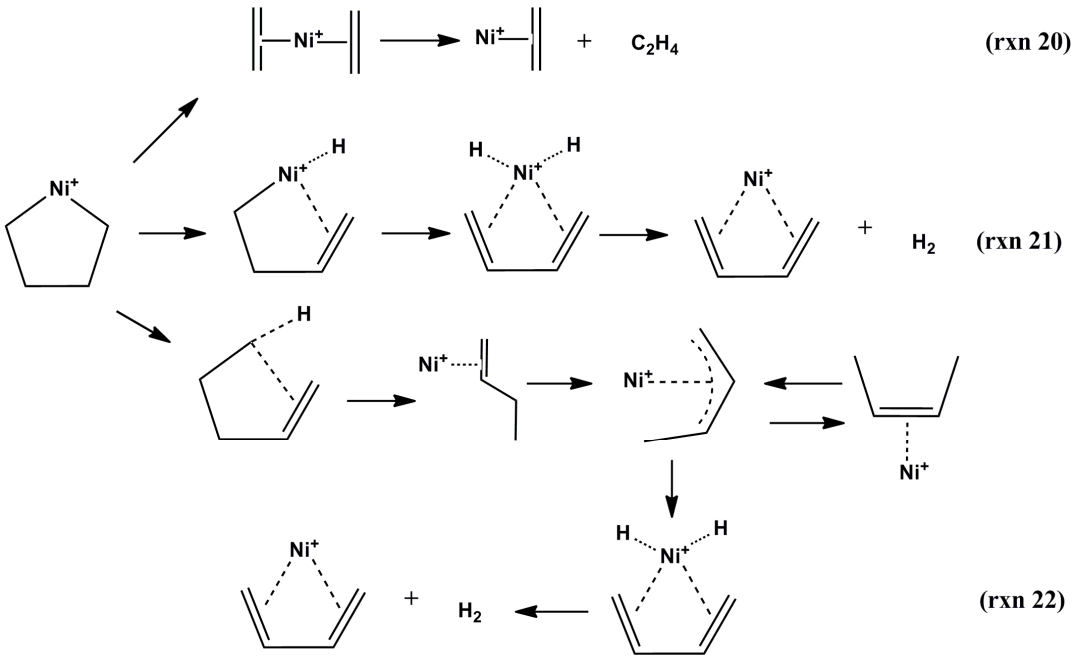


Additional support for rxns 18 and 19 comes from the thermal decomposition of metallacyclopentanes in solution (rxn 20). It is important to note the mechanism proposed by the Freiser[20] group indicates the production of $Ni^+C_2H_4$ instead of $Ni^+CO$. These two fragments ions are indistinguishable in the mass spectrum since they have the same nominal mass (86 amu). The use of cyclopentanone α,α,α',α'-$d_4$ revealed the loss of $C_2H_2D_2$ as the only C-C bond cleavage product for the deuterated metallacycle species.

So far, the Bellert group had studied transition metal ion assisted dissociation of linear ketones[64-66] and aldehydes.[67] These studies have determined the rate limiting step along the reaction coordinate that connects reactants to products. This chapter focuses on preliminary studies regarding the $Ni^+$-assisted decomposition of the cyclopentanone molecule. This is our first study of a ring-opening reaction. This will provide useful

insights into the dynamics of the reaction. This will also allow us to support a previous mechanism or to propose a new dissociative mechanism for this reaction.

*Preliminary Results and Discussion*

$Ni^+$-cyclopentanone ($Ni^+$-Cp) complexes are formed in the same fashion as described in detail in chapter two. Briefly, a focused pulse laser radiation ablates a 0.25 inch diameter nickel rod, thus forming gaseous nickel cations. A high pressure, pulse helium plume, doped with the vapor pressure of cyclopentanone, is timed to entrain and cool the vaporization products through supersonic expansion into vacuum. The interaction between gaseous nickel cations and cyclopentanone vapor ensures the formation of the title complex. The formed complex is skimmed twice before reaching the Willey-McLaren[69] OA. Ions are repelled toward the TOFMS where the common kinetic energy imparted to them allows mass separation. The mass separated ions are finally transmitted through the hemispherical kinetic energy analyzer to strike the MCP detector located at the end of the sector.

Our preliminary studies show the presence of the title complex along with other structures. Figure 22 displays a typical precursor mass spectrum for this study. Although in general the mass spectrum is rather clean and most mass peaks have been assigned, there are some areas where the identity of the mass peaks has not yet been determined. The first two peaks at low mass correspond to the 58 and 60 amu isotopes of $Ni^+$. The next heavier peak corresponds to $Ni^+CO$ or $Ni^+C_2H_4$. Since these two compounds have the same nominal mass they are indistinguishable. Although, the results of Freiser et al.[20] suggest that this fragment corresponds to $Ni^+C_2H_4$ instead of $Ni^+CO$, we are currently unable to confirm this. The peak at mass 114 amu is assigned as the metallacycle

($Ni^+C_4H_8$), which has been previously proposed as a structure in dissociative reaction of $Ni^+Cp$. The major peak is assigned the title complex, $Ni^+Cp$. The high-mass side of the spectrum contains higher order clusters of the title complex. Formation of the larger clusters suggests the significant cooling that takes place during supersonic expansion.

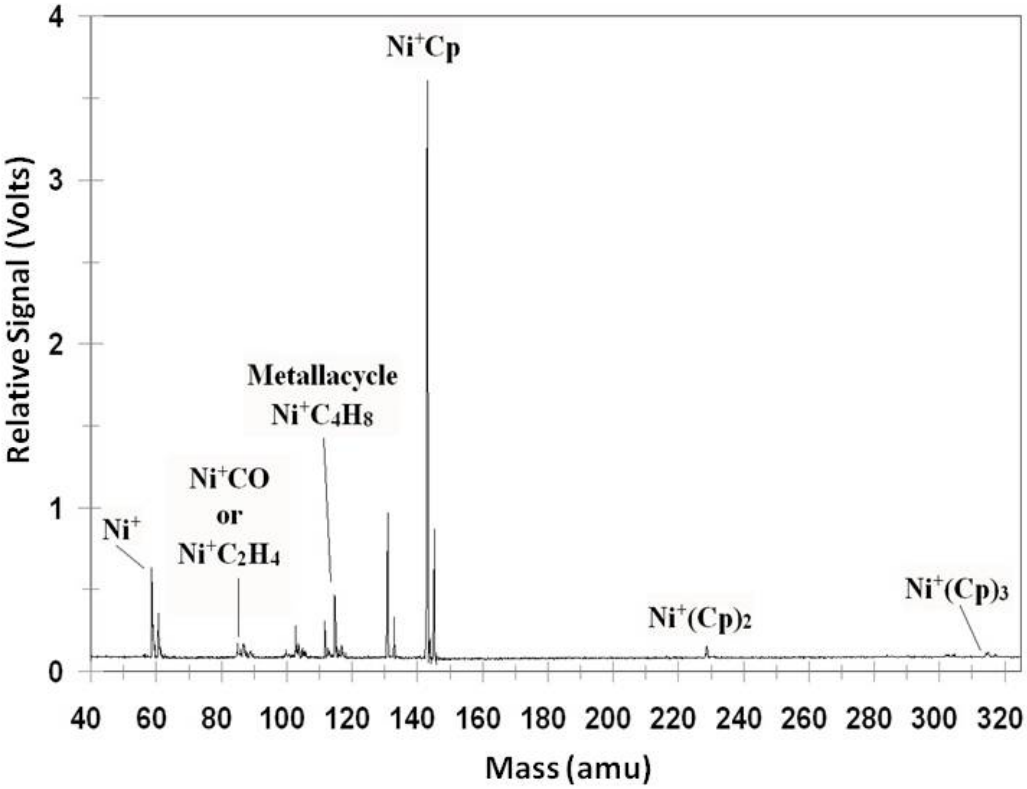


Figure 22. $Ni^+(Cp)$ precursor ion time-of-flight mass spectrum.

Figure 23 displays the fragment ion transmission profile through the sector when a intense, pulsed laser radiation (20 mJ of 16000 $cm^{-1}$, 625 nm) intersects the molecular beam 3 μs before reaching the OA. Intersecting the ion packet at this time ensures that the products monitored result from the relatively slow, reactive decay of the $Ni^+Cp$ cluster. During the reactive decay, single photon absorption initiates the reaction. This provides energy to the cluster so that the $Ni^+$ can cleave bonds and rearrange atoms to

form products. Thus, this process is relatively slow when compared with the fast direct, laser induced dissociation. The identity of the ionic fragments was determined from the potential difference applied across the two sections of the kinetic energy analyzer according to eq.2.1 presented in chapter 2. In Figure 23, two major peaks are observed. The major product is labeled as $Ni^+C_4H_6$ or $Ni^+C_4H_8$. Unfortunately, the resolution of the sector does not allow a sufficient separation between both fragments where the mass difference is 2 amu. Thus, based on previous results,[12, 20] we predict that this major peak actually contains two overlapping peaks. The second peak in the sector voltage scan in Figure 23 is assigned as $Ni^+CO$ or $Ni^+C_2H_4$ since both of these of these fragments have the same mass. However, based on Freiser's[20] deuterium labeled experiments this fragment likely corresponds to $Ni^+C_2H_4$ as is shown in rxn 19. A curious observation in the sector voltage profile is the shape differences between the shoulders of both peaks. The small shoulder observed to the right of the peak at lower voltages is a well-defined peak and corresponds to the $^{60}NiC_2H_4$ fragment. However, the shoulder of the peak at higher voltages presents a tail making it difficult to assign a chemical formula or structure. This supports the conclusion that this peak contains two overlapping fragment peaks. It is noteworthy that there is no transmission of $Ni^+$ which should appear at ~278 V. When photoabsorption occurs prior to right angle extraction in the OA, only fragments from slow reactions can be observed. This suggests that formation of $Ni^+$ results from the direct dissociation of the precursor ion.

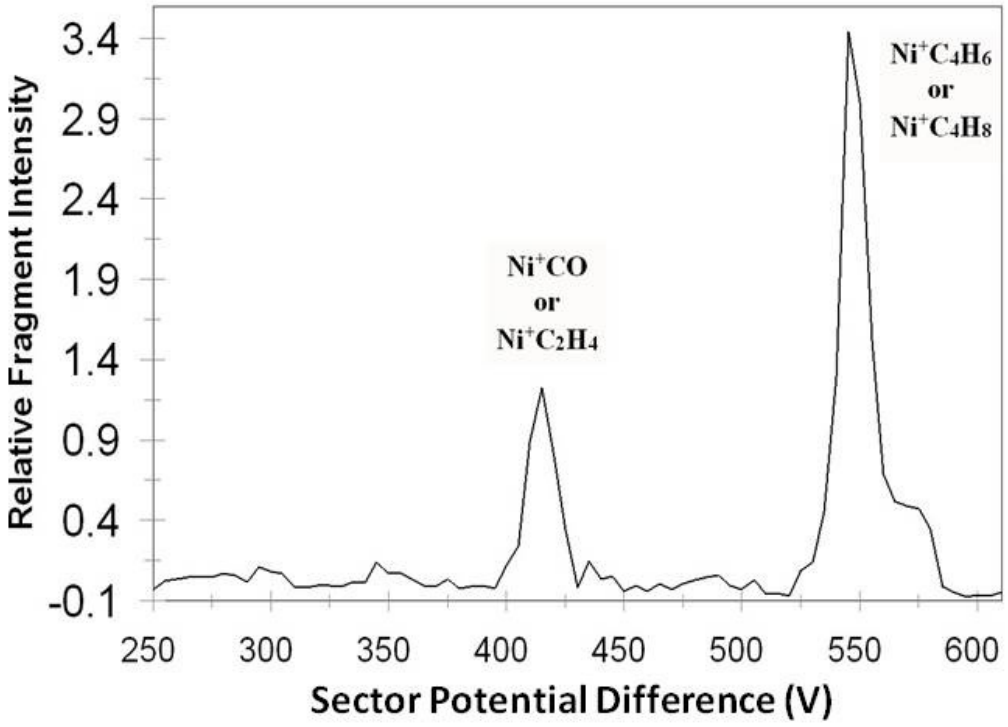


Figure 23. Sector voltage scan of $Ni^+$(Cp) performed at 16000 $cm^{-1}$ of excitation energy.

The nickel cation is responsible for photon absorption in the cluster. The lowest lying electronic excitation in the cyclopentanone molecule is a $\pi^* \leftarrow n$ transition at ~ 32000 $cm^{-1}$.[94] Therefore, $Ni^+$ must act as the chromophore as the electronic transitions in cyclopentanone occur only in the UV. The lowest lying, excited electronic state of $Ni^+$ is a [ $3d^8 4s(^4F)$ ] with the lowest energy spin-orbit component lying at 8394 $cm^{-1}$ above the $Ni^+$ [ $d^9$ ($^2D$) ] ground state (Table 1). According to DFT calculations[82] computed at the B3LYP/6-311++G(d,p) level of theory and zero point energy corrected by our group, the ground electronic state bond energy of the $Ni^+$Cp is ~20500 $cm^{-1}$. This bond is likely formed from the electrostatic attraction between the ground state $Ni^+$ cation and the dipole moment of neutral cyclopentanone.

The photon energy used in these preliminary results is 16000 $cm^{-1}$, which is insufficient to break the $Ni^+$-Cp cluster bond. As described previously the absorption of the photon energy promotes the cluster into excited states that are metastable. Photon emission is forbidden and the complex cannot release energy through bond dissociation, thus, the excited state likely intersystem crosses to the ground potential surface. The photon energy represents the amount of internal energy available for the reaction. Deposition of the absorbed photon energy into the high vibrational levels of the ground state provides the activation energy for the observed reactive dissociation of the cluster ion. The excited cluster will dissociate if the internal energy is in excess of the reaction activation requirements. The precursor concentration follows first order decay, developing in time according to equation 3.1.

Decomposition of $Ni^+$-Cp results in the formation of at least two charged fragments according to the sector voltage scan in Figure 23. However, we are confident that the dissociative reaction yields the three ionic fragments that were proposed by Freiser et al.[20] The percentages of the products are in good agreement with the previous results where the major fragment to minor fragment ratio is ~3.

The masses of two of the charged fragments are too similar to be resolved through our sector ($Ni^+C_4H_8$ and $Ni^+C_4H_6$). Due to this resolution issue, this chapter focuses on the preliminary results from sampling one of those charged fragments: $Ni^+C_2H_4$. The measurement of the dissociation kinetics of cyclopentanone assisted by the nickel cation was performed in the same fashion as described earlier. Briefly, the Nd:YAG pumped dye laser (16000 $cm^{-1}$, 625 nm) radiation is directed toward the counterpropagating molecular beam while selecting the sector to transmit the $Ni^+C_2H_4$ fragment ions. The

intensity of this fragment (integrated through the TOF) is monitored as the timing is varied between trigger commands to fire the OA and the Nd:YAG pumped dye laser. The rate constant is acquired by plotting the natural logarithm of the fragment ion intensity against the time, and extracting the slope through linear regression analysis.

The top panel of Figure 24 displays a dissociative waveform acquired in this fashion. Here, the temporal response of $Ni^+C_2H_4$ production is selectively sampled. The time scale is most conveniently defined as negative time values, and time zero represents the coincident firing of the dye laser and OA. The entire waveform is well described by the exponential character of eq 3.1. The regression constants are used to construct the solid curve through the observed points in the figure. The acquired rate constant is indicated in the figure.

A mechanism for the metal assisted decomposition of cyclopentanone was proposed by Freiser[20] and presented in rxns 7 and 8 in this chapter. Those reactions present a series of elementary steps which show the production of CO, $C_2H_4$ and $H_2$. This mechanism is similar to those presented to describe the metal-assisted decomposition of acetone in previous chapters. It begins with the formation of $Ni^+$-Cp dipole bound encounter complex (EC). The energy of the absorbed photon provides sufficient internal energy so that the $Ni^+$ approaches, and insert into a C-C σ-bond forming the first intermediate. The rate of formation of this inserted complex is governed by the activation rate constant, $k_{act}$. The rate of formation of the second elementary step is governed by the abstraction rate constant, $k_{sft}$, and describes a β-alkyl migration to form a five member ring. The $Ni^+$ is part of this ring and bound to the CO. Following is the step that breaks the interaction between $Ni^+$ and CO to form metallacyclopentane ($k_{prod}$).

The final steps are dehydrogenation and the symmetric cleavage of the ring ($k_{prod}$' and $k_{prod}$'').

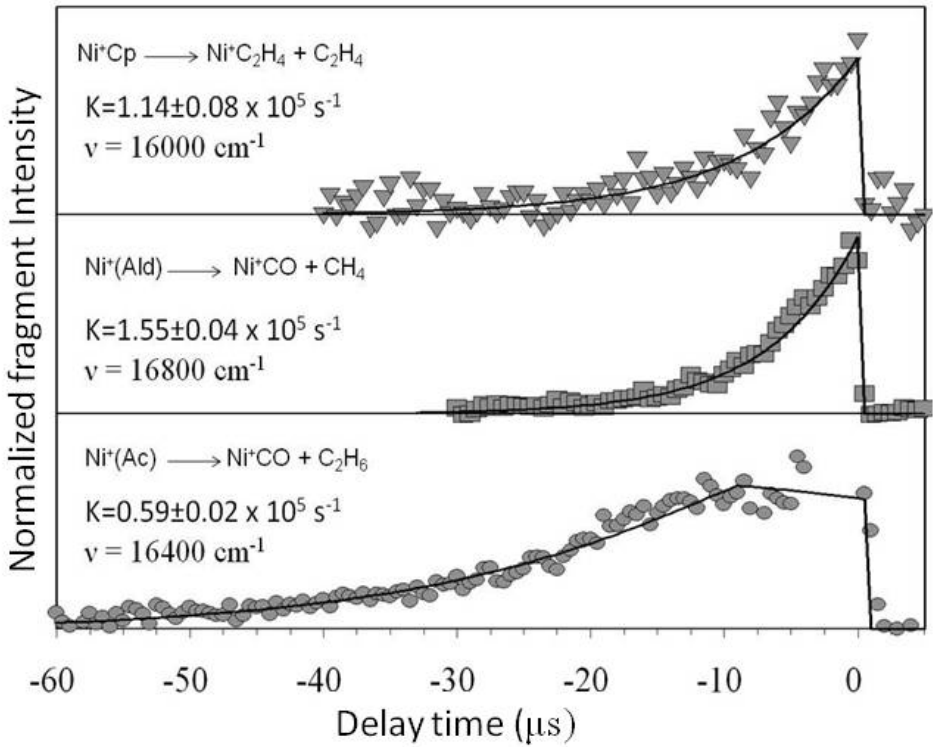


Figure 24. Comparisons between the $Ni^+$ assisted decomposition of cyclopentanone (top panel), acetaldehyde (center panel), and acetone (bottom panel) at similar internal energies. The fragment ion monitored is indicated in each trace as well as the rate constant extracted from each study.

We believe that the $Ni^+$ insertion is the rate limiting step in this decomposition reaction. This is based on comparative studies with similar systems under comparable conditions. The bottom panel of Figure 24 shows the product growth waveform that results from the nickel cation assisted decomposition of acetone upon absorption of 16400 $cm^{-1}$ of energy. As discussed in chapter three, this waveform has a unique shape where at times closer to 0 μs, a plateau forms with nearly unchanging fragment ion intensity. This flat region is caused by an induction period due to the similar valued rate

constants controlling bond activation and rearrangement of the $Ni^+$(Ac) cluster. There are obvious differences in the waveforms provided in the top and lower panels of Figure 24. It appears that a single transition state model will describe the assisted dissociation kinetics of the cyclic ketone. Additionally, the value of the rate constant that limits production of product from cyclopentanone is roughly twice as large as the rate constant that limits the $Ni^+$ assisted decomposition of acetone. Such differences suggest that the induced dissociation dynamics of these ketones are different. We conclude that an alkyl shift is not a kinetically important step in the assisted decomposition of cyclopentanone.

Table 2 displays the rate constants values for the $Ni^+$ activation of C-C bonds in acetone as determined though waveform simulation. The activation rate constant at 16400 $cm^{-1}$ was reported as $1.3x10^5$ $s^{-1}$. This is notably similar to the directly measured rate constant for the nickel cation induced decomposition of cyclopentanone ($1.14x10^5 \pm 0.08$ $s^{-1}$). These similar values suggest a common aspect of the dissociative mechanism. The encounter complex (EC) geometry in both systems has the $Ni^+$ cation loosely aligned with the dipole moment in each ketone. To initiate either decomposition reaction, sufficient energy must be supplied to move the $Ni^+$ cation in opposition to the organic dipolar field, approach, and finally activate the C-C bond. These motions likely have similar activation requirements and will thus have similar rate constants.

The center panel of Figure 24 shows the growth waveform obtained in the $Ni^+$-assisted decomposition of acetaldehyde. In this study[67] we concluded that the decomposition occurs via two parallel paths, aldehyde C-H and C-C σ-bond activation followed by elimination of methane and $Ni^+CO$. At the energy used in Figure 24, the dissociation dynamics of this system are rate limited by bond activation, and the extracted

rate constant is an inseparable combination of C-H and C-C activation. It is obvious that these waveforms have similar shapes and rate limiting rate constants. This comparative study supports our assumption that bond activation is rate limiting in the cyclopentanone decomposition system. However, a single measured value is insufficient to make this conclusive. More experimentation has to be done. Rate constants must be measured at different internal energies (laser energies) as well as measuring the assisted decomposition reaction for the deuterium labeled cyclopentatnone molecule. This will provide measurements of the kinetic isotope effect and assist in assigning the decomposition dynamics.

If C-C σ-bond activation is the rate limiting step in the $Ni^+$ induced dissociation of cyclopentanone, then the rate constants in rxns 18 and 19 can be ordered as $k_{prod} >> k_{sft} > k_{act}$. We assume that the value of $k_{prod}$ should be larger than $k_{sft}$ since this step in the mechanism does not involve significant rearrangement of the cluster prior to dissociation. The magnitudes of these rate constants should inversely scale with the relative energies of the transition state structures. From this assumption and the results of DFT calculation, the semi-quantitative potential energy surface shown in Figure 25 was constructed. Here, the energy of each intermediate structure was minimized at the B3LYP 6-311+G(d, p) level of theory. Calculations of transition state structures and energies were attempted but these failed. Thus, the relative transition state energies were chosen to be consistent with the measured kinetics and assumptions previously stated.

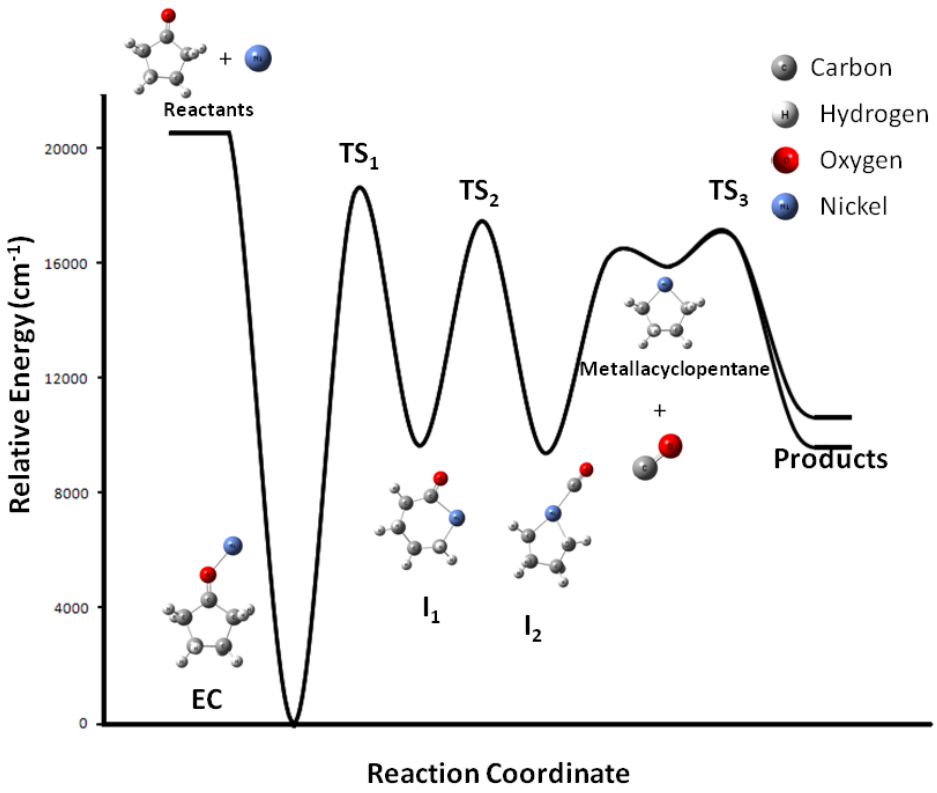


Figure 25. Semi-quantitative potential energy surface for the reaction between the $Ni^+$ cation and the cyclopentanone molecule.

An interesting aspect of this technique is the ability to isolate and measure the decomposition kinetics of various intermediates that occur along the reaction potential energy surface. The metallacyclopentane intermediate has been created in the laser-driven, jet cooled expansion and identified in the mass spectrum of Figure 22. We plan to measure the decomposition kinetics of this intermediate. The decomposition products are shown in reactions 9-11 as well as possible dissociative mechanisms. The product $Ni^+C_2H_4$ offers sufficient mass change to be resolved though our sector and thus provides a handle for this measurement. The magnitude of the rate constant will be compared to those previously obtained for the $Ni^+$ assisted decomposition of cyclopentanone to verify the proposed reaction dynamics.

*Summary*

Preliminary results for the $Ni^+$-assisted decomposition of cyclopentanone has been presented. The rate-limiting reaction rate constant has been measured as k(E= 16000 $cm^{-1}$) = (1.14+/-0.08) x $10^5$) $s^{-1}$. A single state transition model is proposed to describe this dissociative reaction where the rate-limiting step appears to be C-C σ-bond activation.

These preliminary studies represent the group's first ring opening reaction. Additionally, we propose that we can isolate, identify, and measure the reaction kinetics associated with the decomposition of an intermediate. This will be another first for this group and significantly expand upon our current capabilities.

# CHAPTER SIX

## Conclusions

### *General Conclusions*

To conclude, the studies presented here indicate that transition metal ions assist in the dissociation of organic molecules by lowering activation energy barriers. The clusters systems presented here serve as models for the catalytic cleavage of C-C and C-H bonds. This novel technique directly measures the kinetic parameters of dissociative, gas phase reactions at well resolved internal energies. These measurements yield mechanistic information associated with these decomposition processes. Thus far, kinetic and dynamic results for the $Ni^+$ mediated decomposition of linear and cyclic ketones have been acquired. Comparative studies for the $Co^+$ mediated decomposition of acetone and its deuterium analog yielded values for the KIE. These measurements represent the first direct experimental determination of the kinetics for this type of reaction.

One of the most interesting results from this dissertation is the comparative study between the $Co^+$ and $Ni^+$ assisted decomposition of acetone. These two similar systems present rather different dissociation dynamics as evidenced by the measured KIE's. This must be due to the different electronic configurations of each ion and to the low-lying excited state structure. Such differences suggest the important role of electronic structure in catalytic ability. It is hoped that these fundamental studies lead to a better understanding of catalysis and will further the development of commercially viable catalysts.

As a final note, from the study of the $Ni^+$ assisted decomposition of cyclopentanone, these results suggest that the isolation of an intermediate in this decomposition reaction is possible. As a consequence, the direct kinetic determination of an intermediate decomposition can be acquired. This will further the groups experimental technique.

# APPENDIX

# APPENDIX

## Detailed Source Block Design

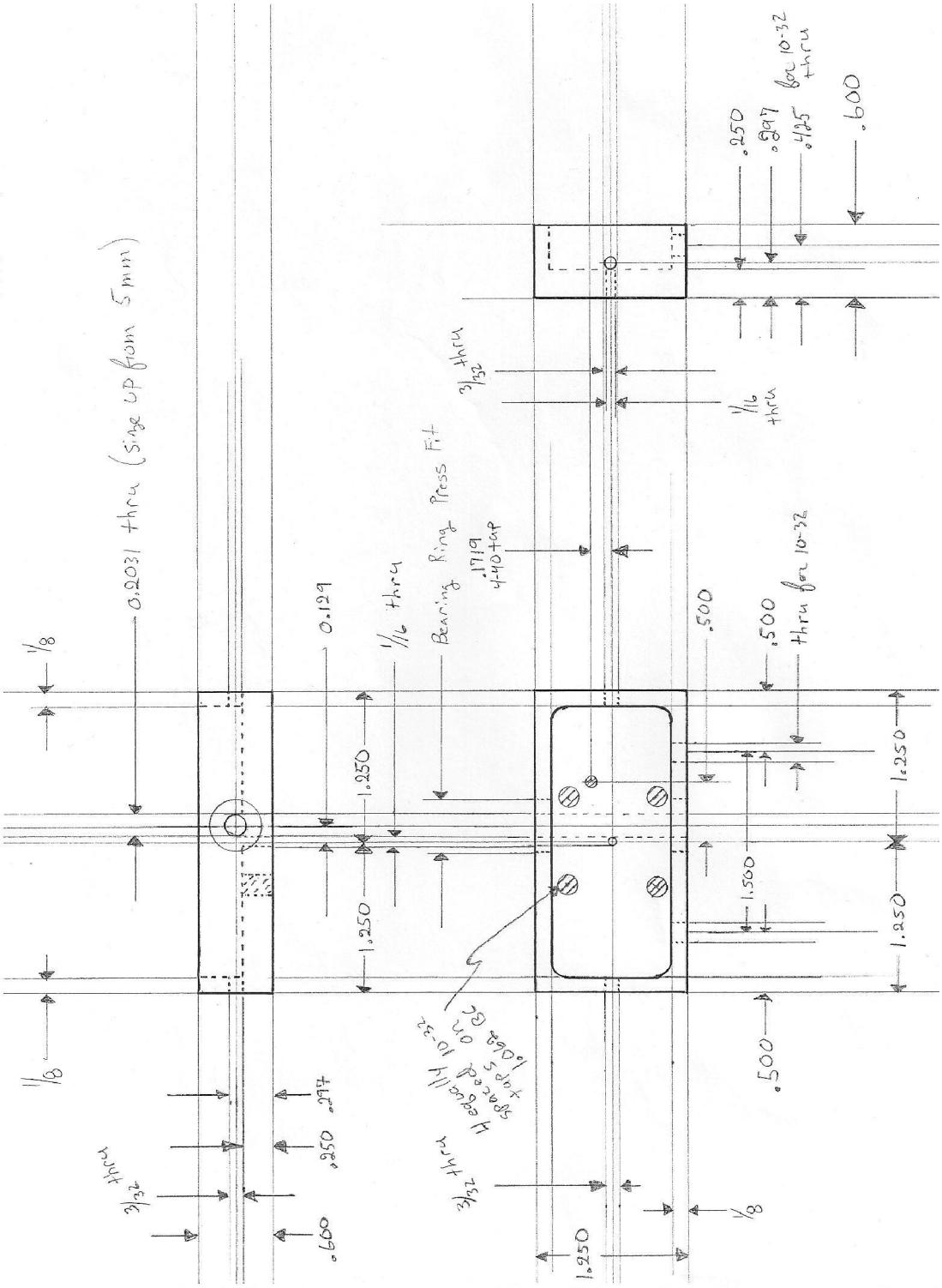


Figure 26. Detailed source block design.

## REFERENCES


1. Allison, J. The Gas-Phase Chemistry of Transition Metal Ions with Organic Molecules In *Progress in Inorganic Chemistry*; Lippard, S.J., Ed.; John Wiley & Sons: New York, 1986; Vol. 34.

2. Beauchamp, J.L.; van Koppen, P.A.M. *NATO ASI Ser., Ser. C.* **1992**, *367*, 287.

3. Hettich, R.L.; Freiser, B.S. Gas-Phase Photodissociation of Transition Metal Ion Complexes and Clusters .In *Fourier Transform Mass Spectrometry*; Buchanan, M.D.V., Ed.; ACS Symposium Series 359; American Chemica Society: Washington, DC, 1987.

4. Buckner, S.W.; Freiser, B.S. In *Gas Phase Inorganic Chemistry;* Russell, D.H., Ed.; Plenum Press: New York, 1989.

5. Dunbar, R.C. In Gas Phase Inorganic Chemistry; Russell, D.H. Ed.; Plenum Press: New York, 1989.

6. Weisshaar, J.C. In Gas-Phase Metal Reactions; Fontijn, A. Ed.; Elservier: Amsterdam, 1992.

7. Operti, L.; Rabezzana, R. *Mass Spectrom. Rev.* **2003**, *22*, 407.

8. Operti, L.; Rabezzana, R. *Mass Spectrom. Rev.* **2006**, *25*, 483.

9. Freiser, B.S. *J. Mass Spectrom.* **1996**, *31*, 703.

10. Organometallic Ion Chemistry. Freiser, B. S. Ed; Kluwer Academic Publishers: Netherlands, 1996, Vol. 15.

11. Roithová, J.; Schröder, D. Chem. Rev. **2010**, *110*, 1170.

12. Halle, F. L.; Houriet, R.; Kappes, M. M.; Staley, R. H.; Beauchamp, J. L. *J. Am. Chem. Soc.* **1982**, *104*, 6293.

13. Halle. L. F.; Crowe, W. E.; Armentrout, P. B.; Beauchamp. J. L. *Organometallics* **1984,** *3,* 1694.

14. Allison, J.; Ridge, D. P. *J. Am. Chem. Soc.* **1977**, *99*, 35.

15. Allison, J.; Ridge, D. P. *J. Organomet. Chem.* **1975**, *99*, C11.

16. Allison, J.; Ridge, D. P. *J. Am. Chem. Soc.* **1976**, *98*, 7445.

17. Hettich, R.L.; Freiser, B.S. *Organometallics* **1989**, *8*, 2447.

18. Burnier, R.C.; Byrd, G.D.; Freiser, B.S. *Anal. Chem.* **1980**, *52*, 1641.

19. Burnier, R.C.; Byrd, G.D.; Freiser, B.S. Anal. Chem. **1981**, *103*, 4360.

20. Jacobson, D.B.; Freiser, B.S. Organometallics **1984**, *3*, 513.

21. Schroder, D.; Schwarz, H. J. Am. Chem. Soc. **1990**, *112*, 5947.

22. Blum, O.; O'Bannon, P.; Schroder, D.; Schwarz, H. Organometallics **1993**, *12*, 980.

23. Schroder, D.; Eller, K.; Prusse, T.; Schwarz, H. Organometallics **1991**, *10*, 2052.

24. Surya, P.I.; Ranatunga, D.R.A.; Freiser, B.S. J. Am. Chem. Soc. **1997**, *119*, 3351.

25. Armentrout, P.B.; Halle, F.L.; Beauchamp, J.L. J. Am. Chem. Soc. **1981**, *103*, 6624.

26. Armentrout, P. B.; Haynes, C. L. Organometallics **1984**, *13*, 3480.

27. Armentrout, P. B.; Beauchamp, J. L. J. Am. Chem. Soc. **1981**, *103*, 784.

28. Jacobson, D. B.; Freiser, B. S. J. Am. Chem. Soc. **1983**, 105, 7484.

29. Jacobson, D. B.; Freiser, B. S. *J. Am. Chem. Soc.* **1983**, *105*, 5197.

30. Laskin, J.; Lifshitz, C. *J. Mass Spectrom.* **2001**, *36*, 459.

31. Hanratty, M. A.; Beauchamp, J. L.; Illies, A. J.; van Koppen, P.; Bowers, M. T. *J. Am. Chem. Soc.* **1988**, *110*, 1.

32. van Koppen, P.A.M.; Brodbelt-Lustig, J.; Bowers, M.T.; Dearden, D.V.; Beauchamp, J.L.; Fisher, E. R.; Armentrout, P.B. *J. Am. Chem. Soc.* **1991**, *113*, 2359.

33. van Koppen, P.A.M.; Bowers, M.T.; Fisher, E. R.; Armentrout, P.B. *J. Am. Chem. Soc.* **1994**, *116*, 3780.

34. Carpenter, C. J.; van Koppen, P. A. M.; Bowers, M. T. *J. Am. Chem. Soc.* **1995**, *117*, 10976.

35. Hanratty, M. A.; Beauchamp, J. L.; Illies, A. J.; van Koppen, P. A. M.; Bowers, M. T. *J. Am. Chem. Soc.* **1988**, *110*, 1.

36. van Koppen, P. A. M.; Brodbelt Lustig, J.; Bowers, M. T.; Dearden, D. V.; Beauchamp, J. L.; Fisher, E. R.; Armentrout, P. B. *J. Am. Chem. Soc.* **1991**, *113*, 2359.

37. van Koppen, P. A. M.; Bowers, M. T.; Fisher, E. R.; Armentrout, P. B. *J. Am. Chem. Soc.* **1994**, *116*, 3780.

38. Halle, L. F.; Armentrout, P. B.; Beauchamp, J. L. *Organometallics* **1982**, *1*, 963.

39. Armentrout, P. B.; Beauchamp, J. L. *Acc. Chem. Res.* **1989**, *22*, 315.

40. Liu, Fuyi,; Zhang, X. G.; Armentrout, P. B. *Phys. Chem. Chem.* Phys. **2005**, *7*, 1054.

41. Sievers, M.R.; Jarvis, L.M.; Armentrout, P.B. *J. Am. Chem. Soc.* **1998**, *120*, 1891.

42. Noll, R. J.; Yi, S. S.; Weisshaar, J. C. *J. Phys. Chem. A* **1998**, *102*, 386.

43. Yi, S. S.; Reichart, E. L.; Weisshaar, J. C. *Int. J. Mass Spectrom.* **1999**, *185/186/187*, 837.

44. Sonnenfroh, D.M.; Farrar, J. M. *J. Am. Chem. Soc.* **1986**, *118*, 3521.

45. Hinrichs, R. Z.; Schroden, J. J.; Davis H. F. Davis H. F. *J. Phys. Chem. A* **2003**, *107*, 9284.

46. Schroden, J. J.; Teo, M.; Davis H. F. *J. Chem. Phys.* **2002**, *117*, 20, 9258.

47. Armentrout, P.B.; Beauchamp, J.L. *J. Am. Chem. Soc.* **1981**, *103*, 6628.

48. Yi, S. S.; Blomberg, M. R. A.; Siegbahn, P. E. M.; Weisshaar, J. C. *J. Phys. Chem. A* **1998**, *102*, 395.

49. Chen,X.; Guo, W.; Zhao, L.; Fu, Q. *Chem. Phys. Lett.* **2006**, *432*, 27.

50. Chen,X.; Guo, W.; Zhao, L.; Fu, Q.; Ma, Y. *J. Phys. Chem.* **2007**, *111*, 3566.

51. Zhao, L.; Zhao, R.; Guo, W.; Lu, X. *Chem. Phys. Lett.* **2006**, *431*, 56.

52. Zhao, L.; Guo, W.; Zhao, R.;. Wu, S.; Lu, X. *Chem. Phys. Chem.* **2006**, *7*, 1345.

53. Zhao, L.; Zhao, R.; Guo, W.; Wu, S.; Lu, X. *Chem. Phys. Lett.* **2005**, *414*, 28.

54. Zhang, Q.; Kemper, P.R.; Bowers, M.T. *Int. J. Mass Spectrom.* **2001**, *210/211*, 265.

55. Allison, J.; Ridge, D. P. *J. Am. Chem. Soc.* **1979**, *101*, 4998.

56. Kinser, R.; Allison, J.; Dietz, T.G.; deAngelis, M.; Ridge, D. P. *J. Am. Chem. Soc.* **1978**, *100*, 2706.

57. Uppal, J. S.; Staley, R. H. *J. Am. Chem. Soc.* **1982**, *104*, 1229.

58. Armentrout, P. B. *Science* **1991**, *251*, 175.

59. Armentrout, P. B.; Beauchamp, J. L. *Acc. Chem. Res.***1989**, *22*, 315.

60. Armentrout, P. B.; Halle, F. L.; Beauchamp, J. L. *J. Am. Chem. Soc.* **1981**, *103*, 6501.

61. Corderman, R.R.; Beauchamp, J. L. *J. Am. Chem. Soc.* **1976**, *98*, 5700.

62. van Koppen, P. A. M.; Kemper. P. R.; Bowers, M. T. Electronic State Effects in Sigma Bond Activation by First Row Transition Metal Ions: The Ions Chromatography Technique.. In Organometallic Ion Chemistry. Freiser, B. S. Ed; Kluwer Academic Publishers: Netherlands, 1996, Vol. 15, pp 157-196

63. Villarroel, O. J.; Laboren, I. E.; Bellert, D.J. *J. Phys. Chem. A* **2011** manuscript in revision.

64. Laboren, I. E.; Villarroel, O. J.; Dee, S. J.; Castleberry, V. A.; Klausmeyer, K.; Bellert, D. J. *J. Phys. Chem. A* **2011**, *115*, 1810.

65. Castleberry, V. A.; Dee, S. J.; Villarroel, O. J.; Laboren, I. E.; Frey, S. E.; Bellert, D. J. *J. Phys. Chem. A* **2009**, *113*, 10417.

66. Dee, S. J.; Castleberry, V. A.; Villarroel, O. J.; Laboren, I. E.; Frey, S. E.; Ashley, D.; Bellert, D. J. *J. Phys. Chem. A* **2009**, *113*, 14074.

67. Dee, S. J.; Castleberry, V. A.; Villarroel, O. J.; Laboren, I. E.; Bellert, D. J. *J. Phys. Chem. A* **2010**, *114*,1783.

68. Ralchenko,Yu., Kramida,A.E., Reader,J., and NIST ASD Team (2011). NIST Atomic Spectra Database (ver. 4.1.0), [Online]. Available: http://physics.nist.gov/asd3 [2011, September 15]. National Institute of Standards and Technology, Gaithersburg, MD.

69. Wiley, W.C; McLaren, I.H. *Rev. Sci. Instrum.* **1955**, *26*, 1150.

70. Laidler, K. J. Chemical Kinetics, 3rd ed; Harper and Row: New York, 1987.

71. Harcourt, A. V.; Esson, *W. Proc. R. Soc. London*, **1865**, *14*, 470.

72. Shimamouchi, T. Tables of Molecular Vibrational Frequencies Consolidated Volume 1; National Bureau of Standards: Washington, DC., 1972; pp 1-160.

73. Hass, Y. *Photochem. Photobiol. Sci.* **2004**, *3*, 6.

74. Goncharov, V.; Herath, N.; Suits, A. G. *J. Phys. Chem. A* **2008**, *112*, 9423.

75. Kemper, P. R.; Bushnell, J.; van Koppen, P.; Bowers, M. T. *J. Phys. Chem.* **1993**, *97*, 1810.

76. Haynes, C. L.; Fisher, E. R.; Armentrout, P.B. *J. Am. Chem. Soc.* **1996**, *118*, 3269.

77. Perry, J. K.; Ohanessian, G.; Goddard III, W. A. *J. Phys. Chem.* **1993**, *97*, 5238.

78. Goebel, S.; Haynes, C. L.; Khan, F. A.; Armentrout, P. B. *J. Am. Chem. Soc.* **1995**, *117*, 6994.

79. Barnes, L.; Rosi, M.; Bauschlisher, C. W. *J. Chem. Phys.* **1990**, *93*, 609.

80. Ma, Y.; Guo, W.; Zhao, L.; Hu, S.; Zhang, J. Fu, Q.; Chen, X. *J. Phys. Chem. A* **2007**, *111*, 6208.

81. van Koppen, P. A. M.; Kemper, P. R.; Bowers, M. T. *J. Am. Chem. Soc.* **1993**, *115*, 5616.

82. Gaussian 03, Revision D.02, Gaussian Inc, 340 Quinnipiac Street, Building 40, Wallingford, CT, 0649; Copyright C 1994-2003, Gaussian, Inc. M. J. Frisch, G. W.Trucks, H. B. Schlegel, G. E. Scuseria, M. A. Robb, J. R. Cheeseman, J. A. Montgomery,Jr., T. Vreven, K. N. Kudin, J. C. Burant, J. M. Millam, S. S. Iyengar, J. Tomasi, V.Barone, B. Mennucci, M. Cossi, G. Scalmani, N. Rega, G. A. Petersson, H. Nakatsuji, M.Hada, M. Ehara, K. Toyota, R. Fukuda, J. Hasegawa, M. Ishida, T. Nakajima, Y. Honda,O. Kitao, H. Nakai, M. Klene, X. Li, J. E. Knox, H. P. Hratchian, J. B. Cross, V. Bakken,C. Adamo, J. Jaramillo, R. Gomperts, R. E. Stratmann, O. Yazyev, A. J. Austin, R.Cammi, C. Pomelli, J. W. Ochterski, P. Y. Ayala, K. Morokuma, G. A. Voth, P. Salvador,J. J. Dannenberg, V. G. Zakrzewski, S. Dapprich, A. D. Daniels, M. C. Strain, O. Farkas,D. K. Malick, A. D. Rabuck, K. Raghavachari, J. B. Foresman, J. V. Ortiz, Q. Cui, A. G.Baboul, S. Clifford, J. Cioslowski, B. B. Stefanov, G. Liu, A. Liashenko, P. Piskorz, I.Komaromi, R. L. Martin, D. J. Fox, T. Keith, M. A. Al-Laham, C. Y. Peng, A.Nanayakkara, M. Challacombe, P. M. W. Gill, B. Johnson, W. Chen, M. W. Wong, C.Gonzalez, and J. A. Pople, Gaussian, Inc., Wallingford CT, 2004.

83. Landis, C. R.; Cleveland, T.; Firman, T. K. *J. Am. Chem. Soc.* **1995**, *117,* 1859.

84. Rosi, M.; Bauschlicher, C. W.; Langhoff, S. R.; Partridge, H. *J. Phys. Chem.* **1990**, *94*, 8656.

85. Perry, J. K.; Goddard, W.A. *J. Chem. Phys.* **1992***, 97*, 7560.

86. Calvert, J.G.; Pitts, J.N. Jr. Photochemistry of the Polyatomic Molecules. In *Photochemistry*; John Wiley & Sons, Inc; New York, 1966; pp 377-410.

87. Srinivasan, R. Photochemistry of the Cyclic Ketones. In *Advances in Photochemistry*; Noyes, W.A. Jr.; Hammond, G.S.; Pitts, J.N. Jr., Eds.; John Wiley & Sons, Inc; New York, 1963; pp 83-113.

88. Saltmarsh, M.; Norrish, R. G. W. *J. Chem. Soc.* **1935**, 445.

89. Bamford, C. H.; Norrish, R. G. W. *J. Chem. Soc.* **1938**, 1521.

90. Srinivasan, R. *J. Am. Chem. Soc.* **1959**, *81*, 1546.

91. Srinivasan, R. J. Am. Chem. Soc. **1961**, *83*, 4344.

92. Srinivasan, R. J. Am. Chem. Soc. **1961**, *83*, 4348.

93. Mok, C. Y. *J. Phys. Chem.* **1970**, *74*, 1432.

94. Furuya, K.; Yamamoto, E.; Jinbou, Y.; Ogawa, T. *J. Electron. Spectrosc. Relat. Phenom.* **1995,** *73,* 59.